



Cite this: *RSC Adv.*, 2023, **13**, 33887

Photodynamic toluidine blue-gold nanoconjugates as a novel therapeutic for *Staphylococcal* biofilms†

Mohammad Okkeh, ^a Lorenzo De Vita, ^b Giovanna Bruni, ^c Lavinia Doveri, ^b Paolo Minzioni, ^d Elisa Restivo, ^{ae} Maddalena Patrini, ^f Piersandro Pallavicini ^{*b} and Livia Visai ^{*ae}

Staphylococci are among the most frequent bacteria known to cause biofilm-related infections. Pathogenic biofilms represent a global healthcare challenge due to their high tolerance to antimicrobials. In this study, water soluble polyethylene glycol (PEG)-coated gold nanospheres (28 ppm) and nanostars (15 ppm) with electrostatically adsorbed photosensitizer (PS) Toluidine Blue O (TBO) \sim 4 μ M were successfully synthesized and characterized as PEG-GNPs@TBO and PEG-GNSs@TBO. Both nanoconjugates and the TBO 4 μ M solution showed remarkable, if similar, antimicrobial photodynamic inactivation (aPDI) effects at 638 nm, inhibiting the formation of biofilms by two *Staphylococcal* strains: a clinical methicillin-resistant *Staphylococcus aureus* (MRSA) isolate and *Staphylococcus epidermidis* (*S. epidermidis*) RP62A. Alternatively in biofilm eradication treatments, the aPDI effects of PEG-GNSs@TBO were more effective and yielded a 75% and 50% reduction in viable count of MRSA and *S. epidermidis* RP62A preformed biofilms, respectively and when compared with untreated samples. This reduction in viable count was even greater than that obtained through aPDI treatment using a 40 μ M TBO solution. Confocal laser microscopy (CLSM) and scanning electron microscope (SEM) images of PEG-GNSs@TBO's aPDI treatments revealed significant changes in the integrity and morphology of biofilms, with fewer colony masses. The generation of reactive oxygen species (ROS) upon PEG-GNSs@TBO's aPDI treatment was detected by CLSM using a specific ROS fluorescent probe, demonstrating bright fluorescence red spots across the surfaces of the treated biofilms. Our findings shine a light on the potential synergism between gold nanoparticles (AuNPs) and photosensitizers in developing novel nanoplatforms to target *Staphylococcal* biofilm related infections.

Received 1st July 2023
 Accepted 19th October 2023

DOI: 10.1039/d3ra04398c
rsc.li/rsc-advances

1. Introduction

Staphylococcus aureus (*S. aureus*) is a highly pathogenic Gram-positive bacterium which is responsible for various kinds of infections, including skin and systemic ones. Following the appearance of methicillin-resistant *S. aureus* (MRSA) strains, a few decades ago, this bacterium has been the subject of intensive studies in the medical field. These strains, as is well-

documented, are able to resist standard antimicrobial therapies.^{1–5} At this point, they account for 40% to 60% of all healthcare-associated infections and are frequent pathogens in the infections of surgical wounds, the dermis and the bloodstream causing sepsis.⁶ *Staphylococcus epidermidis* is the most prevalent skin bacterium, and is often regarded as a contaminant when isolated from infected wounds.⁷ The impact, however, is not limited to the skin as the peptides generated by *S. epidermidis* can contribute to the proliferation of pathogenic bacteria and, as a consequence, antibiotic resistance genes.^{7,8}

S. aureus and *S. epidermidis* can both form biofilms (*i.e.* a clustering of surface-associated microbial cells, enclosed in an extracellular polymeric substance matrix or EPS⁹) which reduce the effectiveness of antimicrobial therapies.^{10–12} The EPS layer acts as a protective barrier against drug entities and cell attacks by the host's innate immune system.¹³ It is reported that sessile bacteria can be as 500–5000 times more antibiotic resistant than their planktonic counterparts.¹⁴

The development of bacterial biofilms, which can form on biotic or abiotic surfaces, as a result of healthcare-associated infections is now one of the most common and most serious

^aDepartment of Molecular Medicine, Center for Health Technologies (CHT), INST UdR of Pavia, University of Pavia, 27100 Pavia, Italy. E-mail: livia.visai@unipv.it

^bDepartment of Chemistry, University of Pavia, 27100 Pavia, Italy. E-mail: piersandro.pallavicini@unipv.it

^cDepartment of Chemistry, Physical Chemistry Section, Center for Colloid and Surfaces Science, University of Pavia, 27100 Pavia, Italy

^dDepartment of Electrical, Computer and Biomedical Engineering, University of Pavia, 27100 Pavia, Italy

^eMedicina Clinica-Specialistica, UOR5 Laboratorio di Nanotecnologie, ICS Maugeri, IRCCS, 27100 Pavia, Italy

^fDepartment of Physics, University of Pavia, 27100 Pavia, Italy

† Electronic supplementary information (ESI) available. See DOI: <https://doi.org/10.1039/d3ra04398c>



complications. This is due to the ease with which biofilms form and the difficulty of treating them afterwards.¹⁵ There is, as a consequence, an urgent need for novel therapeutic approaches, and ones which go beyond those based on traditional antibiotics.

Light-induced therapies including photodynamic therapy (PDT) and photothermal therapy (PTT), along with sonodynamic therapy (SDT) have shown very promising results as potent therapeutics for global health-care challenges such as cancer,^{16,17} and multidrug resistant (MDR) bacteria.¹⁸ Photodynamic therapy (PDT) is a minimally invasive methodology which is used to kill cancerous, bacterial or other types of cells by laser irradiation.^{19,20} It works by activating a photosensitizer (PS), using a light source of a wavelength which is compatible with the PS absorption spectrum, in the presence of oxygen.^{21,22} The interaction between the PS and the light generates free radicals and reactive oxygen species (ROS) which, in turn, leads to cell death, through the deleterious oxidative effects on intracellular molecules, such as RNA, DNA, proteins and lipid molecules.^{22,23} The particular benefits of employing PDT as an antimicrobial therapy are that (a) it is equally effective against antibiotic resistant microbial cells²⁴ and (b) it is engineered to reduce the likelihood of the development of microbial resistance to PDT in the sense that the photo-destructive effects of ROS act at multiple bacterial sites, reduces the likelihood of developing resistance.²⁵ Toluidine Blue O (TBO) is a cationic phenothiazine dye which is well studied as an antibacterial photosensitizing agent.²⁶⁻³⁰ It is able to generate cytotoxic singlet oxygen when excited at a suitable wavelength (596–665 nm),³⁰⁻³² is able to form cations when solubilized in water and is low cost.²⁹ These factors make it an attractive choice as an alternative antimicrobial therapeutic.

Nanoparticles (NPs) have recently emerged both as promising antimicrobial agents themselves and as carriers for other antimicrobial agents: this is due to their unique physicochemical properties and, in particular, to a large surface area-to-volume ratio which facilitates interaction with microbial membranes.³³ Although nanoparticles made from a number of different materials have been discussed and reviewed, gold nanoparticles (AuNPs) are of considerable interest. This is due to their stability, biocompatibility, pharmacokinetic characteristics³⁴ and antimicrobial activity.^{35,36}

It has been reported that the use of metal-based photosensitizing NPs as PS carriers (a process which combines the hyperthermic, antimicrobial and optical properties of metal material with the photodynamic activity of PS)³⁷⁻³⁹ outperformed PS alone in terms of phototoxicity against mammalian and microbial cells.⁴⁰

This study reports our work on PEGylated gold nanostars (PEG-GNSs) and gold nanospheres (PEG-GNPs), which were prepared, characterized, and electrostatically functionalized with the photosensitizer TBO. The prepared nanoconjugates were tested and compared to assess the efficiency of their antimicrobial photodynamic inactivation (aPDI) actions in inhibiting biofilm formation, and their ability to reduce bacterial viability on 24 hour preformed biofilm cultures of two *Staphylococcal* biofilm producing strains: a clinical MRSA

isolate and a *S. epidermidis* RP62A. Scanning electron microscope (SEM) and confocal laser scanning microscopy (CLSM) were used to characterize the aPDI actions of the prepared nanoconjugates against both bacterial strains, in biofilm inhibition and eradication treatments.

2. Materials and methods

2.1 Materials

The following were purchased from Sigma-Aldrich (Milan, Italy) and were used without further purification: gold(III) chloride trihydrate (~30 wt% in HCl 99.99%) MW: 339.79 g mol⁻¹, sodium borohydride (98%), L-ascorbic acid (AA) (≥99%), silver nitrate (99.8%), sodium citrate (≥99%), hydrochloric acid (≥37%), nitric acid (1 N), TritonTM X-100, ethanol (≥99.7%), HS-PEG-COOH mw 5000, thiazolyl blue tetrazolium bromide (MTT), toluidine blue O (~80%) MW: 305.83 g mol⁻¹, D(+)-glucose (≥99.5%), sodium chloride (≥99.0%). CellROX[®] Deep Red and Hoechst 33342 solution were purchased from Thermo Fisher Scientific (Milan, Italy). All reagents were used as received.

The following instruments were used in the study: UV-vis spectrophotometer (HJ1908003 Auromere, Italy), Zetasizer Nano (ZS90 Malvern, UK), ClariostarTM microplate reader (BMG-Labtech, Germany), shaker incubator (CertomatTM BS-T, B. Braun Biotech International, Germany), lyophilizer (Emitech K-850 apparatus, UK), Zeiss EVO-MA10 scanning electron microscope SEM (Carl Zeiss Microscopy GmbH, Germany), transmission electron microscope TEM (Jeol JEM-1200 EX II instrument, Italy), pH meter (Thermo Fisher Scientific, Italy), inductively coupled plasma optical emission spectroscopy ICP-OES (OPTIMA 3000 PerkinElmer instrument, Italy), TA instruments thermogravimetric analyzer (TGA) Q5000, Thermo Scientific Nicolet iS20 FTIR Spectrometer, atomic force microscopy (AFM) with a SmartSPM microscope (Horiba Scientific), and ultracentrifuge (Beckman L7-65, USA).

2.2 Methods

2.2.1 Synthesis of gold nanospheres (GNPs) and gold nanostars (GNSs)

2.2.1.1 Glassware pre-treatment. Before any synthesis involving nanoparticles, the glassware was rinsed with bi-distilled water and then cleaned by filling it with aqua regia (3 : 1 v/v HCl 37% and HNO₃ 65%) for 20 min, after which the oxidant mixture was removed, and the glassware were filled with bi-distilled water and sonicated for 3 min. Water washing and sonication were repeated 2 more times. The purpose of this purification procedure was to remove any trace elements of metal ions.⁴¹

2.2.1.2 GNPs synthesis. GNPs were prepared with the standard Turkevich method.⁴¹ Briefly, 87 μL of a 1.44 M tetrachloroauric acid (HAuCl₄) solution in water were added to 500 mL of boiling Milli-Q water. The heat was then switched off and 25 mL of a 1.7×10^{-2} M sodium citrate dihydrate solution in water were added, under magnetic stirring. The synthesis was considered complete after a further 2 hours of stirring. The total Au concentration in the final solution was 2.4×10^{-4} M.



2.2.1.3 GNSs synthesis. The GNSs were prepared following a seed growth procedure, previously described.⁴² Briefly, seeds were prepared in a vial by mixing 5.0 mL of a Triton X-100 aqueous solution (0.2 M) and 5.0 mL of a tetrachloroauric acid solution (HAuCl₄) aqueous solution (4.5×10^{-4} M). Then 600 μ L of an ice-cooled solution of NaBH₄ in water (0.01 M) were quickly added to the pale-yellow solution of HAuCl₄ obtained in the previous step. The resulting brown-orange solution was gently hand-shaken for a couple of seconds. This solution contained small spheroidal NPs ($d < 5$ nm) that are the seeds. It was stored in an ice bath and needed to be used within 3 hours. The growth solution was prepared starting from 50 mL of 0.2 μ M Triton X-100 solution in water and adding, in this precise order and under magnetic stirring: 2500 μ L of AgNO₃ in water (0.004 M), 50 mL of aqueous HAuCl₄ (4.5×10^{-4} M), and 1600 μ L of an aqueous L-ascorbic acid solution (0.0788 M). This process yielded a colourless solution after few seconds of gentle mixing. After this, 120 μ L of the seed solution were added, during which the suspension could be observed turning from pink to purple and blue and, finally, to a grey-blue colloid suspension. At this point, the mixing was stopped. The colloidal suspensions were stored in the preparation flask in the dark, ready for the PEGylation (*i.e.*, coating with a thiol-functionalized polyethylene glycol).

2.2.1.4 HS-PEG-COOH coatings. The GNSs and GNPs were stabilized by grafting a thiolated polyethylene glycol (HS-PEG) of a high molecular weight on their surface. We used HS-PEG-COOH (MW 5000), with a thiol at one end and a carboxylic acid function on the other end of the chain.

The GNSs and GNPs were coated by adding HS-PEG-COOH (MW 5000) to a flask of either GNSs or GNPs colloidal solutions and stirred overnight. The thiol PEG concentration was 2.0×10^{-5} M. Synthesis impurities and excess HS-PEG-COOH after coating were removed with three cycles of ultracentrifugation for 40 min at 15 093 $\times g$. After the third centrifugation phase, the pellets were resuspended in Milli-Q water, centrifuged again, and then finally resuspended in 100 mL of Milli-Q water in a flask stored at 2–8 °C. The actual Au molar concentration of both colloidal solutions of PEG-GNSs and PEG-GNPs was measured by oxidizing a small volume with aqua regia and with inductively coupled plasma optical emission spectroscopy (ICP-OES). PEG-GNPs and PEG-GNSs suspensions were filter sterilized (0.45 μ M) and then UV sterilized for 30 min prior to the antibacterial assays. The measured concentrations for PEG-GNPs and PEG-GNSs suspensions, as detected by ICP-OES, were 28 ppm and 30 ppm respectively.

2.2.2 TBO adsorption onto PEG-GNPs and PEG-GNSs. A stock solution of 1 mM toluidine blue (TBO) was prepared in Milli-Q water, filter sterilized (0.22 μ m) and stored in a fridge at 2 to 8 °C in the dark. When used, the stock solution was appropriately diluted in sterile Milli-Q water to obtain the desired concentration.

The toluidine blue moiety was electrostatically adsorbed on both types of PEGylated gold nanoparticles PEG-GNSs and PEG-GNPs. This was done by mixing a certain volume of a known concentration of either PEG-GNSs or PEG-GNPs with the same

volume of a known concentration of TBO solution (on a 1:1 ratio) in a falcon tube. The resulting suspensions were mixed overnight using a rotator mixer to allow for TBO electrostatic adsorption (Fig. 1A and B: the –COOH groups of HS-PEG-COOH are deprotonated and negatively charged at neutral pH) and the products were later purified by ultra-centrifugation and by redispersion processes. We used a UV-visible spectrometer to measure the adsorbed quantity of TBO molecules at the polymer surface of the PEG-AuNPs. The UV-visible absorption spectra of the resulting supernatants allowed for the detection of the unabsorbed quantity of TBO Table 1. Based on a previously determined standard curve of TBO absorbance at 634 nm Fig. S1,[†] and a comparison with molar concentration levels, we were able to indirectly calculate the amount of adsorbed TBO on PEG-GNPs and PEG-GNSs. The centrifuged pellets were then redispersed in sterile Milli-Q water.

2.2.3 Physicochemical characterization of GNPs and GNSs.

The morphology of the AuNPs was observed by a transmission electron microscope TEM Jeol JEM-1200 EX II instrument (Jeol Italia SPA, Italy) using 10 μ L samples, deposited on nickel grids (300 mesh) covered with a parlodion membrane. The hydrodynamic diameter and ζ -potential measurements of the AuNPs, before and after functionalization, were determined with a Zetasizer Nano (model: ZS90 Malvern, UK). The UV spectrums for AuNPs before and after functionalization were monitored by recording the spectrum between 400 and 700 nm (GNPs) and then between 600 and 1000 nm (GNSs), using a UV spectrophotometer (model: HJ1908003 Aurogene, Italy). UV spectroscopic and hydrodynamic diameter measurements were monitored for a 30 day period, with measurements at three timepoints (day 0, 7 and 30) to evaluate the nanoconjugates stability. Thermogravimetric analysis (TGA) on PEG-GNPs and PEG-GNS was carried out using a TA Instruments Q5000 instrument on 1–3 mg solid samples obtained from ultracentrifugation of large volumes and drying of the pellets. Fourier-transform infrared spectroscopy (FTIR) analysis was carried out with a Nicolet iS20 (Thermo Scientific) equipped with a DTGS detector working in a spectral range of 4000–600 cm^{-1} , with a resolution of 2 cm^{-1} . A total of 32 scans were collected to obtain a high signal-to-noise ratio.

2.2.4 Laser system setup for aPDI. We used a 638 nm continuous wave (CW) laser diode with a nominal maximum output power of 194 mW (source L638P200, controlled using driver LDC 205B and temperature controller TED 200C, all from Thorlabs Inc.). The culture plates were irradiated from the top up, as illustrated in (Fig. 2I and II), with a light intensity of 194 mW cm^{-2} .

2.2.5 Bacterial strains and culture conditions. The micro-organisms used in this study were *Staphylococcus epidermidis* RP62A [PMID: 3679536], and a clinical isolate of methicillin-resistant *Staphylococcus aureus* MRSA. The *S. epidermidis* RP62A [PMID: 3679536] sample, a biofilm-producing strain, was kindly provided by Professor T. J. Foster (Department of Microbiology, Dublin University, Dublin, Ireland) and the MRSA sample was provided by Professor Migliavacca (Department of Microbiology at the University of Pavia, Pavia, Italy). Bacteria were routinely grown in a tryptic soy broth (TSB) (Difco



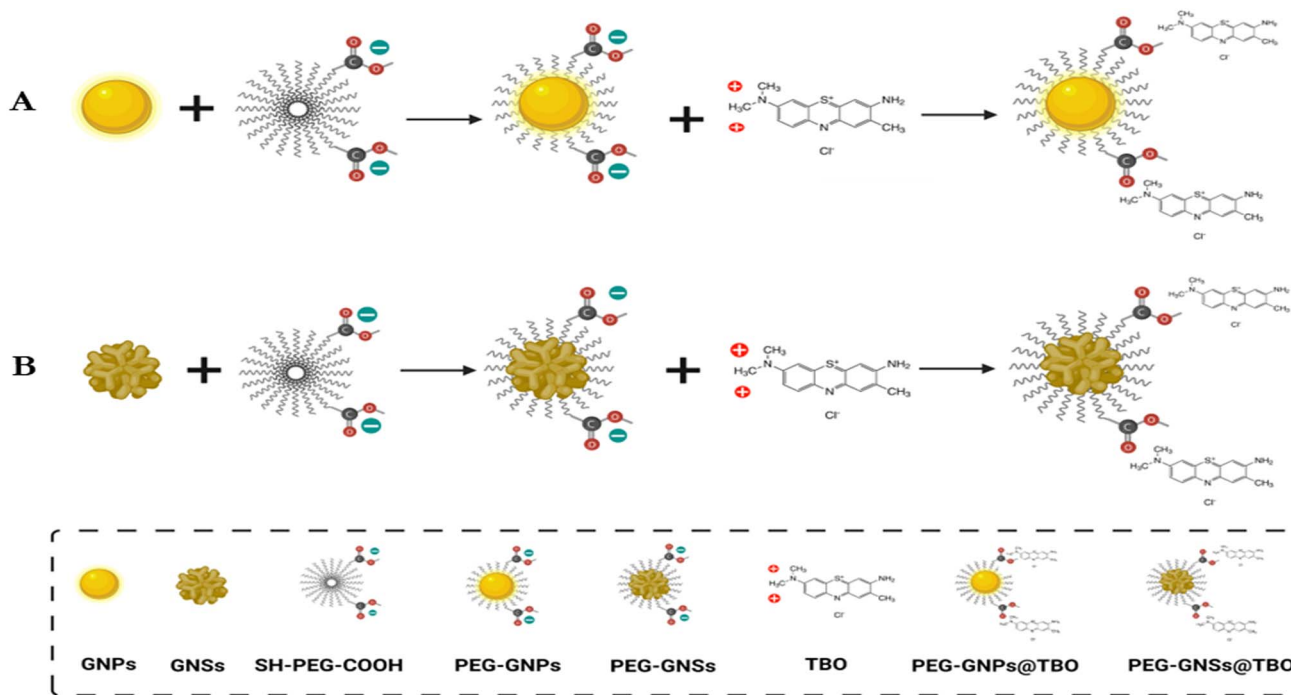


Fig. 1 PEG-GNPs@TBO and PEG-GNSs@TBO synthesis scheme. Schematic illustration for the coating process of [A] GNPs and [B] GNSs with HS-PEG-COOH, and afterwards their electrostatic conjugation with TBO molecules. Abbreviations: GNPs: gold nanospheres, GNSs: gold nanostars, TBO: toluidine blue O, HS-PEG-COOH: thiolated polyethylene glycol with carboxylic acid end moiety (schematic illustration created with <https://BioRender.com>).

Laboratories Inc., Detroit, MI, USA) under aerobic conditions and at a temperature of 37 °C with a shaker incubator (model: Certomat™ BS-T, B. Braun Biotech International, Germany) at 200 rpm.

2.2.6 *In vitro* antibiofilm assays

2.2.6.1 *Biofilms treatment with PEG-GNPs and PEG-GNSs.* The experiments were performed under two treatment conditions for both bacterial strains: biofilm inhibition and eradication treatments.

Biofilm inhibition treatments:

The dose-dependent effects of PEG-GNPs and PEG-GNSs on biofilm formation were determined using the twofold broth microdilution method. A double-strength medium (100 µL) of TSB broth was used to fill the wells in the first column of a 48-well plate to compensate for the first dilution. The other wells were filled with single-strength TSB medium (100 µL). A 100 µL volume of the highest concentration of either PEG-GNPs or PEG-GNSs suspensions were added to the first column. Double fold serial dilutions were then carried out across the plate in

three successive steps. The bacteria, overnight-grown, were diluted in a 0.25% glucose-supplemented TSB medium to 4×10^4 CFU mL⁻¹. Then, 100 µL of the diluted bacterial suspension was added to the geometric dilutions of PEG-GNP or PEG-GNS suspensions inside the 48-well plate (1 : 1 ratio) and the plates were incubated for a 24 hour period at 37 °C. The untreated samples (positive controls) consisted of a 100 µL single strength TSB medium mixed with 100 µL of diluted bacterial suspensions as previously mentioned.

The supernatants, containing planktonic cells, and the PEG-GNS or PEG-GNP suspensions were carefully removed after incubation. At this point, bacterial biofilm formations was assessed by Crystal Violet (CV) assay, as described by Christensen *et al.*⁴³ Briefly, the biofilms were washed twice with sterile phosphate-buffered saline (PBS) (0.134 M NaCl, 8.34 mM Na₂HPO₄, 1.64 mM NaH₂PO₄, pH 7.4) to remove the planktonic cells. Then, the cells were fixed with 96% ethanol for 10 min and stained with 0.1% crystal violet for 15 min. After several washings, the wells were air dried. For a quantitative estimation of

Table 1 Quantity of electrostatically conjugated TBO to PEG-GNPs@TBO/PEG-GNSs@TBO. TBO's quantity was estimated indirectly through the measurement of unbound TBO in the supernatant of TBO and PEG-GNPs/PEG-GNSs mixtures see Fig. S1. Data were expressed as mean \pm standard deviations ($n = 3$)

Type of nanoconjugate	Quantity of TBO conjugated to PEGylated gold nanoparticles (µM)	Measured absorbance of TBO left in the supernatant after conjugation
PEG-GNPs@TBO	4.023 ± 0.030	0.177 ± 0.001
PEG-GNSs@TBO	4.007 ± 0.084	0.176 ± 0.004



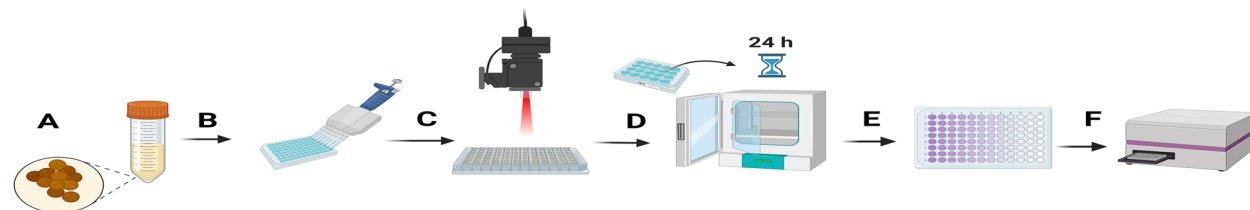
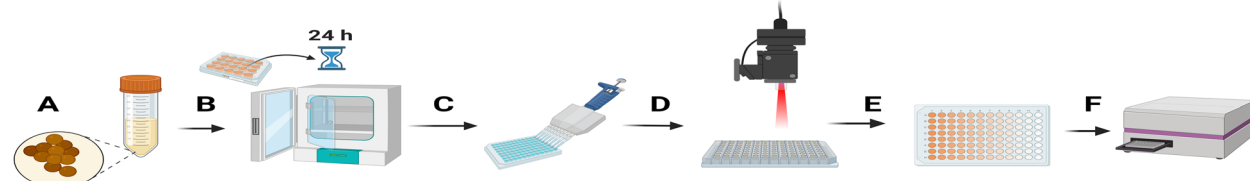
I) Biofilm inhibition treatment**II) Biofilm eradication treatment**

Fig. 2 Schematic illustration for the experimental setup of biofilm inhibition and eradication treatments: [I] biofilm inhibition treatments: (A) overnight bacteria culture, (B) seeding bacteria into culture plate with the addition of treatments afterwards, (C) laser irradiation, (D) incubation for 24 hours at 37 °C to induce biofilms formation, (E) crystal violet assay for biofilm formations detection, (F) reading CV absorbance values at 590 nm using the microplate reader. [II] Biofilm eradication treatments: (A) overnight bacteria culture, (B) incubation for 24 hours at 37 °C to induce biofilms formation, (C) treatments addition to the preformed biofilms, (D) laser irradiation, (E) MTT assay to detect bacterial viability after treatments, (F) reading solubilized formazan salts absorbance values at 570 nm using the microplate reader (schematic illustration created with <https://BioRender.com>).

biofilm formation, crystal violet was solubilized with 10% glacial acetic acid. The absorbance of the solubilized dye was determined at 590 nm by a Clariostar™ microplate reader (BMG-Labtech, Germany). The percentage of biofilm formation was calculated by dividing the CV absorbance intensity of the treated bacterial samples by the CV absorbance intensity of bacteria grown in the untreated samples.

Biofilm eradication treatments:

200 μ L of *S. epidermidis* RP62A or MRSA cultures at 5×10^6 CFU mL⁻¹ in 0.25% glucose supplemented TSB medium were seeded in a 48-well plate for 24 hours at 37 °C.

At the end of the incubation period the supernatant containing planktonic cells were carefully removed and 200 μ L of PEG-GNs or PEG-GNP suspensions, already diluted by a 0.25% glucose-supplemented TSB medium, were added to the formed biofilms which were incubated for a further 24 hours at 37 °C. 200 μ L of a 0.25% glucose-supplemented TSB medium were added to the untreated samples (positive controls). At the end of the incubation period, the supernatant containing the PEG-GNPs or PEG-GNPs suspensions, along with the planktonic cells, was carefully removed and the biofilms were washed once with a sterile PBS.

The formed biofilms were vigorously disrupted, and the bacterial cell viability was assessed through the quantitative 3-[4,5-dimethylthiazol-2-yl]-2,5-diphenyltetrazolium bromide (MTT) assay as previously reported.⁴⁴ This colorimetric assay measures dehydrogenase activity as an indicator of the bacterial metabolic state. MTT, dissolved in sterile PBS (0.134 M NaCl, 8.34 mM Na₂HPO₄, 1.64 mM NaH₂PO₄, pH 7.4), was prepared at 5 mg mL⁻¹ (stock solution) and diluted within the well plate at 0.5 mg mL⁻¹ for the viability tests. Reduction of the MTT salt, mediated by cellular respiration, results in purple insoluble

formazan granules that are dissolved through acidified 2-propanol (0.04 M HCl). Absorbance spectrophotometric values were read using Clariostar™ microplate reader (BMG-Labtech, Ortenberg, Germany) at 570 nm. The surviving fraction was calculated by dividing the number of viable bacteria after treatments by the number of viable bacteria in untreated samples. Following the same procedure, we also investigated the antibacterial effect of TBO solutions against MRSA and *S. epidermidis* RP62A biofilm cultures, as reported in ESI (Fig. S6A†).

2.2.6.2 Biofilms aPDI treatments with PEG-GNPs, PEG-GNPs@TBO, PEG-GNPs, PEG-GNPs@TBO suspensions and TBO solution. Biofilms of both bacterial strains were treated with PEG-GNPs, PEG-GNPs@TBO, PEG-GNPs, PEG-GNPs@TBO suspensions or TBO solutions and were exposed to laser under two different treatment conditions: biofilm inhibition and eradication treatments.

Biofilm inhibition treatments:

100 μ L of *S. epidermidis* RP62A or MRSA cultures at 4×10^4 CFU mL⁻¹ in 0.25% glucose supplemented TSB medium were seeded in a 48-well plate. 100 μ L of PEG-GNPs, PEG-GNPs@TBO, PEG-GNPs, PEG-GNPs@TBO suspensions or TBO solutions, already diluted in 0.25% glucose-supplemented TSB medium, were added to the bacterial cultures (1 : 1 ratio). 100 μ L of 0.25% glucose-supplemented TSB medium were mixed with 100 μ L of diluted bacterial cultures (1 : 1 ratio) in untreated samples (positive controls). The samples were divided into two groups: those treated in dark conditions and those treated with laser exposure (~ 0.2 W cm⁻² at 638 nm for 15 min). At the end of the irradiation process, both irradiated and non-irradiated samples were incubated at 37 °C for 24 hours. At the end of the incubation period, CV assay was conducted to reflect the



biofilm formation profile, following the same procedure indicated in biofilm inhibition treatments in Section 2.2.6.1.

Biofilm eradication treatments:

Bacterial cultures of each strain were seeded in a 48 well-plate for 24 hours at 37 °C to induce biofilm formation, as mentioned in Section 2.2.6.1. After removing the supernatant, and washing with sterile PBS, 200 µL of PEG-GNPs, PEG-GNPs@TBO, PEG-GNSs, PEG-GNSs@TBO suspensions or TBO solutions were carefully added to the preformed biofilms and were incubated for 1 hour at 37 °C. 200 µL of sterile Milli-Q water were added to untreated samples (positive controls). At the end of the incubation period, the samples were divided into two groups: those treated in dark conditions and those treated with laser exposure ($\sim 0.2 \text{ W cm}^{-2}$ at 638 nm for 15 min). At the end of the irradiation process, the surviving fraction of bacterial cells in both groups was evaluated by MTT assay, as described in Section 2.2.6.1.

2.2.6.3 Scanning electron microscopy (SEM) and atomic force microscopy (AFM) imaging. Biofilm inhibition treatments:

A 400 µL volume containing 200 µL ($4 \times 10^4 \text{ CFU mL}^{-1}$) of either *S. epidermidis* RP62A or MRSA cultures and 200 µL of either PEG-GNSs, or PEG-GNSs@TBO suspensions diluted in a 0.25% glucose supplemented TSB medium (1 : 1 ratio) was seeded on Thermanox™ coverslips (Nunc) which had been placed inside 24-well plates. The untreated samples (positive controls) consisted of a 400 µL final volume containing 200 µL ($4 \times 10^4 \text{ CFU mL}^{-1}$) of either *S. epidermidis* RP62A or MRSA cultures and 200 µL of a 0.25% glucose supplemented TSB medium (1 : 1 ratio). The samples were divided into two groups: those treated in dark conditions and those treated with laser exposure ($\sim 0.2 \text{ W cm}^{-2}$ at 638 nm for 15 min). After irradiation, the samples were incubated for a 24 hour period at 37 °C, followed by a fixation process. The supernatant was carefully removed, and the samples were fixed with 2.5% (v/v) glutaraldehyde in a 0.1 M Na-cacodylate buffer, pH 7.2, for 1 hour at 4 °C. After additional washes with cacodylate buffer, to remove the excess of glutaraldehyde, the samples were incubated using increasing concentrations of ethanol (25, 50, 75, and 96%) for 10 min. They were then dried to the critical point using a lyophilizer (Emitech K-850 apparatus, UK) and placed on a mounting base. The last step involved attaching coverslips on aluminium stubs with a C bi-adhesive tape and sputtered with gold (3 times for 1 min at 10 mA). Analysis was carried out using a Zeiss EVO-MA10 scanning electron microscope (Carl Zeiss Microscopy GmbH, Germany) with an acceleration voltage of 20 kV at a working distance of 8.5 mm. A scale bar was inserted using ImageJ software.

Biofilm eradication treatments:

400 µL ($5 \times 10^6 \text{ CFU mL}^{-1}$) of either *S. epidermidis* RP62A or MRSA cultures in 0.25% glucose-supplemented TSB medium were seeded on Thermanox™ coverslips (Nunc), already inside the 24-well plates, and were incubated for 24 hours at 37 °C. After incubation, the supernatant containing planktonic cells was carefully removed, and 400 µL of PEG-GNSs or PEG-GNSs@TBO suspensions were carefully added to cover the biofilm on the sterile coverslip. The samples were incubated for 1 hour at 37 °C prior to laser irradiation. 400 µL of sterile Milli-Q

water were carefully added to untreated samples (positive controls).

Samples were divided into two groups: those treated in dark conditions and those treated with laser exposure ($\sim 0.2 \text{ W cm}^{-2}$ at 638 nm for 15 min). After irradiation, the samples were fixed following the procedure described in the paragraph above. For (AFM) imaging, the biofilm morphology of the same samples was analyzed by tapping mode Atomic Force Microscopy (AFM) with a SmartSPM microscope (Horiba Scientific), with NT-MDT NSG03 tips (resonance frequency 110 kHz, radius 10 nm). Images were taken from 70 µm to 4 µm scale, with scan rate 1 Hz and were processed through IPro software analysis.

2.2.6.4 Confocal laser scanning microscopy (CLSM) imaging.

For confocal studies performed in biofilm eradication treatments, 400 µL ($5 \times 10^6 \text{ CFU mL}^{-1}$) of either *S. epidermidis* RP62A or MRSA cultures in 0.25% glucose-supplemented TSB medium, were seeded on sterile glass coverslips placed inside 24-well plates and were incubated for 24 hours at 37 °C. After incubation, the supernatant containing planktonic cells was carefully removed, and 400 µL of PEG-GNSs or PEG-GNSs@TBO suspensions were carefully added to cover the biofilm on the sterile coverslip. The samples were incubated for 1 hour at 37 °C. 400 µL of sterile Milli-Q water was carefully added to untreated samples (positive controls). Samples were divided into those which were laser irradiated ($\sim 0.2 \text{ W cm}^{-2}$ at 638 nm for 15 min) and those which were kept at dark conditions. After laser treatment, the supernatant containing the nanoconjugate suspensions for both groups were carefully removed and the biofilms were carefully washed, once, with sterile PBS. The viability of the bacterial cells in treated biofilms was monitored using the LIVE/DEAD® BacLight bacterial viability kit L7012. This kit uses two fluorescent nucleic acid stains: SYTO9 and propidium iodide. SYTO9 permeates both living and dead bacteria. Propidium iodide, on the other hand, permeates only bacteria with damaged membranes and quenches SYTO9 fluorescence. The dead bacteria, which are penetrated by propidium iodide, fluoresce red whereas the viable bacteria fluoresce green. To assess viability, 1 µL of the stock solution of each stain was added to 3 mL of sterile PBS and, after mixing, 400 µL of the prepared solution was dispensed into the 24-well plates containing the biofilms grown on the sterile glass coverslips. The culture plates were incubated at 37 °C for 15 min in the dark. Stained bacteria were analysed with a Leica CLSM (model TCS SP8 DLS; Leica, Wetzlar, Germany) with a 40× oil immersion objective. The excitation and emission wavelengths used for monitoring SYTO9 were 488 and 525 nm, respectively. Propidium iodide was excited at 520 nm, and its emission was monitored at 620 nm. The 3D projections and scale bar were generated using LAS X software.

2.2.6.5 ROS detection. The semi-quantitative assessment of ROS generation in biofilm eradication treatments was assessed with the fluorescent probe CellROX® Deep Red reagent. This probe is a cell-permeable reagent that is localized within the cytoplasm. It is non-fluorescent or very weakly fluorescent while in a reduced state and upon oxidation exhibits a strong red fluorescent signal. For the induction of biofilms, and their consecutive treatments with the PEG-GNSs or PEG-GNSs@TBO



suspensions we followed the same experimental process reported above (Section 2.2.6.4) but used the CellROX® Deep Red reagent instead of the LIVE/DEAD® BacLight bacterial viability test. CellROX® Deep Red reagent, at a final concentration of 5 μM , was added to the formed biofilms and was incubated in dark conditions for 30 minutes at 37 °C. After incubation, the probe was carefully removed, and the biofilms were washed twice with sterile PBS. Then the biofilms were fixated with 3.7% formaldehyde for 15 minutes. After fixation, a nuclear counterstain Hoechst 33342 solution at a concentration of 20 μM was added to all the samples. Hoechst 33342 (2'-[4-ethoxyphenyl]-5-[4-methyl-1-piperazinyl]-2,5'-bi-1H-benzimidazole trihydrochloride trihydrate) is a cell-permeable DNA stain that is excited by ultraviolet light and emits blue fluorescence at 460 to 490 nm. Stained bacteria were examined with a Leica CLSM (model TCS SP8 DLS; Leica, Wetzlar, Germany) using a $63\times$ oil immersion objective. The excitation and emission wavelengths used for monitoring CellROX® Deep Red were 640 and 665 nm, respectively. Hoechst 33342 was excited at 460 nm, and emission was observed at 490 nm. The images and the scale bar were generated using software LAS X. Mean of corrected total cell fluorescence (CTCF) was calculated using ImageJ software as follows: CTCF = integrated density – (area of selected cells \times mean fluorescence of background). The mean fluorescence of the background was collected using areas without fluorescence adjacent to bacterial cells.

2.2.7 Statistical analysis. The experiments were performed with $n = 3$. All data measurements were represented as mean \pm standard deviations (SDs). To identify statistically significant differences between groups, one-way variance analysis (ANOVA) was performed, followed by Bonferroni post hoc, for multiple comparisons or Student's *t*-test to compare the means between two groups (significance level of $p \leq 0.05$). All the statistical calculations related to antibacterial tests were carried out using

GraphPad Prism 9.0 (GraphPad Inc., San Diego, CA, United States).

3. Results and discussion

3.1 Physicochemical characterization of GNPs and GNSs

GNPs were prepared by the Turkevich method,⁴¹ *i.e.* by reducing HAuCl₄ with excess sodium citrate in Milli-Q water. In our measurements of the UV spectral band, we observed the expected sharp localized surface plasmon resonance (LSPR) absorption band typical of small gold nanospheres GNPs, with $\lambda_{\text{max}} = 520$ nm, (Fig. 3A), imparting the typical intense purple-red colour to the colloidal solutions.

TEM imaging confirmed the expected spheroidal shape of the prepared GNPs, (Fig. 3B), with an average diameter of 17 (± 1) nm. The hydrodynamic diameter (d_h) was 26.3 (± 0.8) nm (Fig. 3G), with a zeta-potential of -31.5 ± 0.7 mV (average of 3 measurements) due to the citrate coating, at the pH of the synthesis (~ 5.7) (Fig. 3C).

Dynamic light scattering (DLS) control experiments were carried out on d_h at different pH values, finding almost unchanged dimensions at 9.0 ($d_h = 29.5 \pm 1.5$ nm) and 7.4 ($d_h = 26.1 \pm 0.4$ nm), while at pH 3 the strong acid (HCl) addition promoted aggregation ($d_h = 40.0 \pm 1.8$ nm).

The GNSs, on the other hand, were prepared according to a synthetic pathway optimized in our laboratory,⁴² utilizing a seed-growth process involving Triton X-100 surfactant, as a shape-directing and protecting agent, and AgNO₃ in small amounts ($\sim 10\%$ molar ratio *vs.* Au) to further direct the anisotropic growth.

The synthetic parameters used yielded GNSs with 5–6 branches and with a tip-to-tip maximum distance of 80–120 nm, as can be seen in the transmission electron microscope (TEM) images (Fig. 3E). These GNSs have multiple LSPR absorption

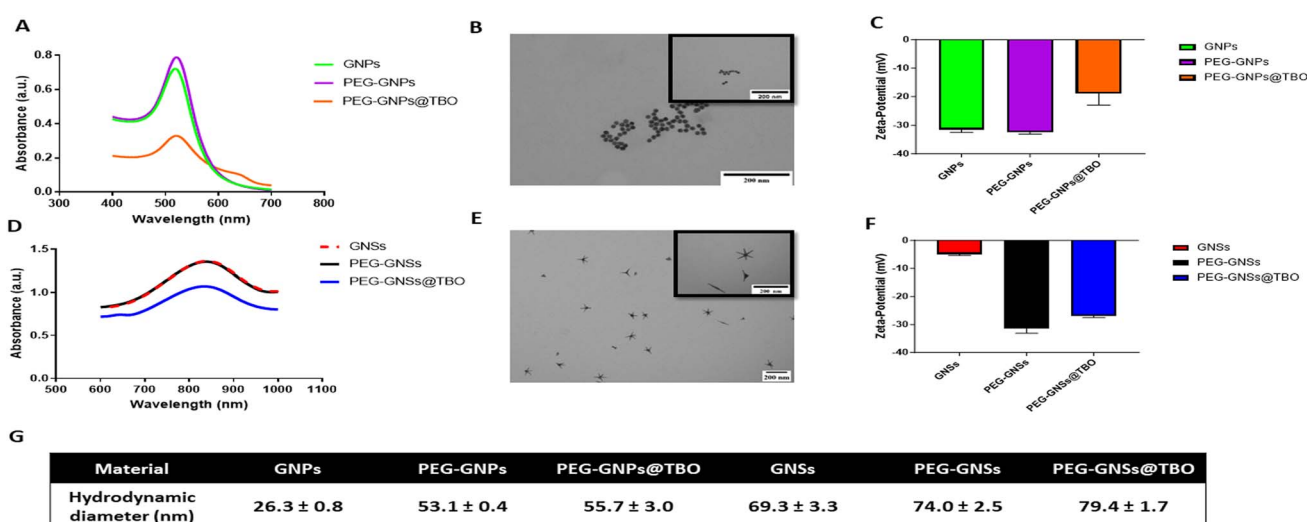


Fig. 3 Physicochemical characterization of GNPs and GNSs suspensions. UV-vis absorption spectra of GNPs [A] and GNSs [D]; TEM images of GNPs [B] and GNSs [E] (TEM scale bar: 200 nm); zeta-potential measurements of GNPs [C] and GNSs [F]; hydrodynamic diameter measurements of GNPs and GNSs suspensions at the pH of synthesis [G]. Data were expressed as mean \pm standard deviations ($n = 3$). TEM images [within the black frames] represent specific sections from the same corresponding images at a larger magnification.

bands, dominated by two very intense peaks whose maximum can be tuned, changing the synthetic conditions, to between 750 and 1100 nm (LSPR1) and 1200 and 1600 nm (LSPR2), respectively. In this study, we obtained the LSPR1 band placed between 830 and 850 nm as shown in (Fig. 3D). A good reproducibility of the synthetic procedure can be noticed by comparing the absorption spectra recorded on different batches (Fig. S2†). The zeta-potential of the GNSs samples was almost neutral, *i.e.* -5 ± 0.3 mV (average of 3 measurements) at the pH of synthesis ~ 3 (Fig. 3F), due to the non-ionic nature of the adsorbed Triton X-100 surfactant. The hydrodynamic diameter of the as-synthesized GNSs was 69.3 ± 3.3 nm (Fig. 3G). DLS control experiments at pH 7.4 and 9.0 did not show significant changes, with $d_h = 68.0 \pm 4.6$ nm and 72.8 ± 4.6 nm, respectively.

The prepared GNPs and GNSs were coated with COOH-PEG-SH MW 5000, as shown graphically (Fig. 1A and B). The weakly bound coating citrate for GNPs and the Triton X-100 for GNSs, were easily replaced by an α -thiolated polyethylene glycol bearing an Ω -carboxylic acid function (COOH-PEG-SH 5000). Considering that a -COOH function is fully deprotonated at pH > 6 , PEGylation of the AuNPs was essential to ensure stability in water.⁴⁵ This is necessary for the electrostatic adsorption of the cationic TBO molecules onto the negatively charged surfaces of the PEG-GNPs or PEG-GNSs suspensions and, in addition, prevents aggregation and so further enhances stability.⁴⁶ Moreover, PEG grafting on GNSs ensures that excess amounts of Triton X-100, a cytotoxic substance, are removed. Finally, PEGylation prevents the severe product loss that may be caused by repeated ultracentrifugation cycles on uncoated GNPs and GNSs.⁴⁷ PEGylation resulted in a small red shift (2–3 nm) of the LSPR band peak for both GNPs and GNSs (Fig. 3A and D). The hydrodynamic diameters of both PEG-GNPs and PEG-GNSs increased upon surface decoration (with COOH-PEG-SH 5000). Considering the acidic nature of the coating, we measured such parameter at pH 3.0, 7.4 and 9.0, finding 50.7 ± 1.8 , 53.1 ± 0.4 , and 54.7 ± 1.5 nm, respectively, in the case of PEG-GNPs, and 87.0 ± 2.8 , 74.0 ± 2.5 , 76.1 ± 2.2 nm, respectively, in the case of PEG-GNSs. The slight differences found between acidic (pH 3.0) and basic conditions (pH 7.4 and 9.0) are to be attributed to the -COOH group, that is neutral at pH 3.0 and fully deprotonated at basic pH, this inducing minimal changes in the interactions between vicinal PEG chains and on their overall conformation. Moreover, an additional slight increase was also detected upon the adsorption of TBO molecules, on the PEG-GNSs or in the PEG-GNPs suspensions (Fig. 3G). In addition, the effective surface charge (*i.e.* zeta potential) changed on functionalization with COOH-PEG-SH 5000. Again, due to the ionizable nature of the -COOH group, this parameter was measured at pH 3.0, 7.4 and 9.0, obtaining -10.4 ± 0.3 , -32.4 ± 0.8 and -38.7 ± 2.1 mV, respectively, for PEG-GNPs, and -8.7 ± 0.3 , -31.4 ± 1.7 , -35.9 ± 1.3 mV, respectively, for PEG-GNSs. For the aims of this paper, it is relevant to stress that at pH ~ 7.4 the zeta-potential changes only slightly on PEGylation of the citrate-coated GNPs, remaining strongly negative. On the other hand, it shifts from -5 mV to -31 mV for GNSs, as the neutral Triton X-100 is replaced by the deprotonated COOH-PEG-SH 5000 polymer.

The PEG-GNPs and PEG-GNSs suspensions were both ultracentrifuged 3 times to remove synthesis impurities and excess amounts of citrate and Triton X-100 and were filter sterilized ($0.45 \mu\text{m}$) prior to mixing with TBO solution. This resulted in losing a certain quantity of PEG-GNPs and PEG-GNSs, as is evident from the UV-vis absorption spectrums of PEG-GNPs@TBO and PEG-GNSs@TBO (Fig. 3A and D).

Further characterization of the PEGylated PEG-GNPs and PEG-GNSs was carried out by Thermogravimetric analysis (TGA) (Fig. S3†). For PEG-GNPs TGA revealed a 10.65% mass loss due to COOH-PEG-SH 5000 decomposition, to be compared with a 4.44% mass loss for the parent citrate-coated GNPs. For PEG-GNSs, a 14.78% mass loss was found, *vs.* a 2.88% for the parent GNSs. FT-IR analysis (Fig. S4B†) shows a significant difference between the citrate-coated GNPs obtained from synthesis (that has a weak and almost featureless spectrum) and PEG-GNPs. The latter display the rich set of signals typical of a polyethylene glycol. The difference in the FT-IR spectra of GNSs and PEG-GNSs is instead less evident, due to the presence of Triton X-100 around the as-synthesized GNSs, a molecule that has structural similarities with PEG.

Following the successful PEGylation, TBO was adsorbed into the polymer surface of the PEG-GNSs or PEG-GNPs suspensions by electrostatic interaction, as indicated in (Fig. 1A and B). Mixing TBO solution with the PEGylated AuNPs increased zeta-potential values for both PEG-GNPs@TBO and PEG-GNSs@TBO suspensions, conforming that electrostatic adsorption of the cationic TBO molecules onto the anionic polymer surface of PEG-GNPs and PEG-GNSs had taken place (Fig. 3C and F). The increase in zeta-potential value was more pronounced in the PEG-GNPs@TBO samples than in the PEG-GNSs@TBO samples. This is likely because PEG-GNPs are smaller and more uniformly sized than PEG-GNSs. These morphological factors might have distributed the oppositely charged TBO molecules onto the negatively charged polymer surface of PEG-GNPs more evenly and, as a result, increased the net surface charge of the polymer surface. Additionally, looking at the UV graphs provided in Fig. 3A and D we can observe a small peak at 634 nm, which also confirms the conjugation of TBO.

The stability of the PEG-GNPs@TBO and PEG-GNSs@TBO suspensions were evaluated as indicated in (Fig. 4). We monitored the stability of the nanoconjugate suspensions by taking three different measurements, over a month-long period, of UV-vis absorption spectra and hydrodynamic diameters (Fig. 4A, B and D). Samples were stored in a fridge between 2 and 8 °C throughout the testing period. By means of these measurements, which exhibited little variation, we were able to confirm that the nanoconjugates remained stable over the course of test period. Visual examination of the nanoconjugate suspensions showed no aggregation nor a change in colour (Fig. 4C), which agrees with the other evaluations of stability.

3.2 aPDI effects on biofilm formations by treatments with PEG-GNPs@TBO and PEG-GNSs@TBO

Before assessing the aPDI effect of PEG-GNPs@TBO and PEG-GNSs@TBO on biofilm formation of both bacterial strains

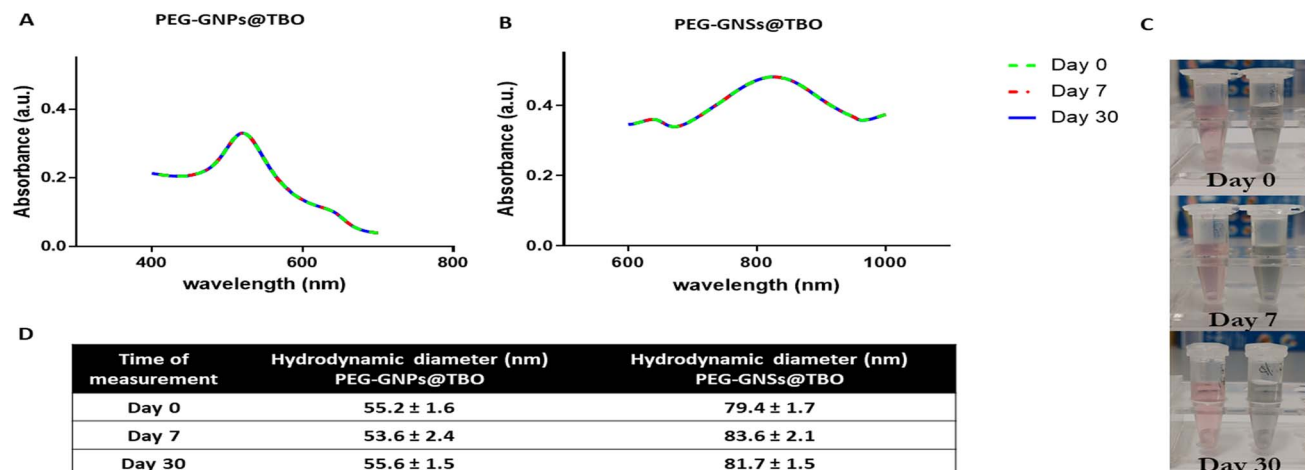


Fig. 4 Stability evaluation of PEG-GNPs@TBO and PEG-GNSs@TBO suspensions. UV-vis absorption spectra of PEG-GNPs@TBO [A] and PEG-GNSs@TBO [B] recorded at different times as indicated. PEG-GNPs@TBO (light rose eppendorf) and PEG-GNSs@TBO (light grey eppendorf) suspensions images taken at different times as indicated [C]. Hydrodynamic diameter measurements of PEG-GNPs@TBO and PEG-GNSs@TBO recorded at different times as indicated [D].

(Fig. 6), a preliminary assessment was made of the effect of PEG-GNPs and PEG-GNSs without conjugated TBO (Fig. 5).

PEG-GNPs and PEG-GNSs, at different concentrations, were tested for their intrinsic biofilm inhibition effect against planktonic cultures of the biofilm-producing Gram positive bacterial strains MRSA and *S. epidermidis* RP62A.³⁰ The crystal violet CV biofilm assay showed an increment in the biofilms inhibition effect for both types of PEG-AuNPs against both

bacterial strains as shown in (Fig. 5A and B) as well as the corresponding CV well-plate images in (Fig. 5C and D). For PEG-GNSs the biofilm inhibition effect plateaued after 15 ppm, and 30 ppm for MRSA and *S. epidermidis* RP62A cultures, respectively. Instead for PEG-GNPs, the gradual increase in dose correlated with an increased inhibition in biofilm formation, for both bacterial strains. Although AuNPs are generally considered to be biologically inert, and do not to possess

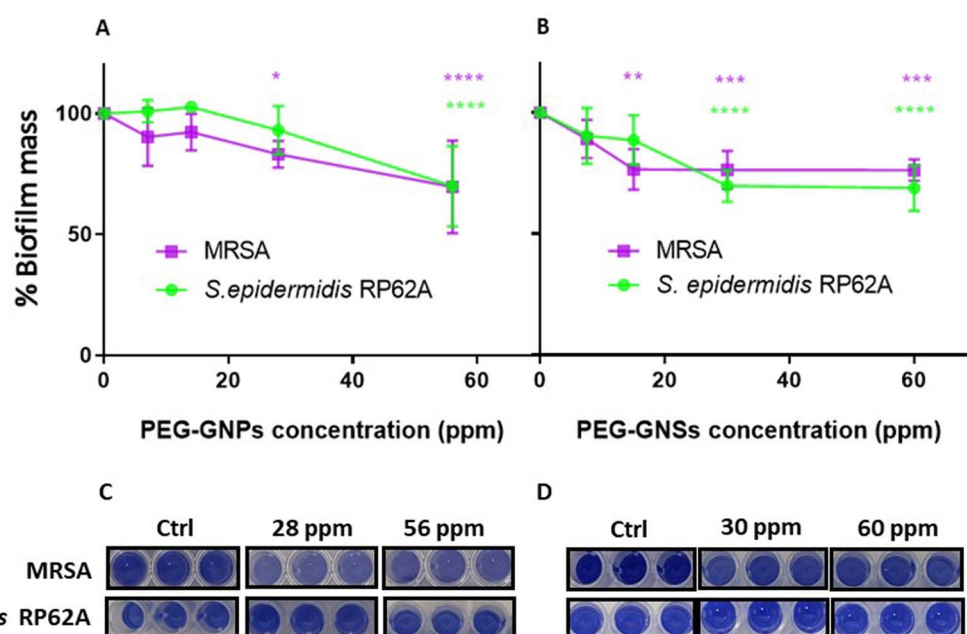


Fig. 5 Dose-dependent effects of PEG-GNPs and PEG-GNSs on *Staphylococcal* biofilm formations. To evaluate the intrinsic dose-dependent effect of PEG-GNPs [A and C] and PEG-GNSs [B and D] on biofilm formations by MRSA and *S. epidermidis* RP62A planktonic cultures, CV assay was performed. Percentage of biofilm mass formation was calculated as indicated in Materials and methods in Section 2.2.6.1. Data were expressed as mean ± standard deviations ($n = 3$). Test groups were compared to the untreated samples using one-way variance analysis (ANOVA), followed by Bonferroni post hoc, for multiple comparisons where: * $p < 0.05$, ** $p < 0.01$, *** $p < 0.001$, **** $p < 0.0001$. [C and D] Qualitative images of bacterial biofilm biomass stained with CV after incubation with PEG-GNPs [C] and PEG-GNSs [D], compared to the control.



antibacterial properties,⁴⁸ a number of studies have indicated that there are ways in which AuNPs, of various shapes and dimensions, can in fact exert an intrinsic antibacterial activity. Small spherical AuNPs, for example, can produce holes in the bacterial cell wall, leading to the loss of cell contents and eventually cell death.^{49,50} These studies explain the gradual decrement in the ability of both MRSA and *S. epidermidis* RP62A cultures to form biofilms after being incubated with incremental doses of PEG-GNPs. It has also been demonstrated elsewhere, in other work on GNSs, that the larger quasi-spherical and star-shaped AuNPs can adhere on bacterial cells, causing membrane stretching and rupturing.^{51,52}

Another contributing factor to the antibacterial effect of GNSs could be the presence of silver ($\sim 10\%$) in the GNSs lattice, added during the synthesis phase:⁴² the gradual release of small quantities of Ag^+ ions from the GNSs suspension, when incubated with bacteria, may well account for this cytotoxic effect against bacterial cells.⁵³ Other papers have highlighted the potential of AuNPs to directly impact the bacterial respiratory chain through nicotine amide³⁵ or through the generation of reactive oxygen species (ROS) and the induction of oxidative stress.⁵⁴

In our study, we argue that the dose-dependent decrease in biofilm formation is in fact due to a reduction in the bacterial cell count which occurs as a result of the physical interaction between the bacterial planktonic cells of either MRSA or *S. epidermidis* RP62A with either the PEG-GNPs or PEG-GNSs.

We are able to exclude the possibility that this antibacterial effect is in any way due to synthesis impurities or excess reactants, as reported previously,⁵⁵ since three rounds of ultracentrifugation were conducted for the PEG-GNPs and PEG-GNSs suspensions before the antibacterial assays.

Based on the results of the intrinsic biofilm inhibition effect of our PEG-GNPs and PEG-GNSs suspensions (Fig. 5), we chose to proceed with our aPDI evaluations using PEG-GNPs and PEG-GNSs suspensions concentrations that exhibited a lower intrinsic biofilm inhibition effect. The concentrations that were chosen, as measured by ICP-OES, were as follows: $[\text{Au}] \sim 28 \text{ ppm}$ for PEG-GNPs and $\sim 15 \text{ ppm}$, for PEG-GNSs. The same concentrations were used for the adsorption of TBO molecules onto the polymer surface of PEG-GNPs and PEG-GNSs suspensions, and later for the subsequent antibacterial assays.

The amount of adsorbed TBO on the PEG-GNPs@TBO and PEG-GNSs@TBO samples was indirectly measured by UV-vis absorption spectroscopy (Section 2.2.2) and it was found to be similar for both nanoconjugates. Approximately $\sim 4 \mu\text{M}$ of TBO (an average of 3 measurements) was found to be electrostatically attached to PEG-GNPs [28 ppm] and PEG-GNSs [15 ppm]. A possible explanation for the attachment of a similar amount of TBO $\sim 4 \mu\text{M}$ for both PEG-GNPs and PEG-GNSs despite the differences in their measured $[\text{Au}]$ concentrations is the fact that PEG-GNSs are larger in size than PEG-GNPs (Fig. 4). In the remaining antibacterial evaluations described in this study, the antibacterial activity of nanoconjugates was compared with the antibacterial activity of a $4 \mu\text{M}$ TBO solution as this effectively mirrors the amount that was adsorbed onto the polymer surface of the nanoconjugates. Our objective was to evaluate and compare the differences in antibacterial activity of PEG-

GNPs@TBO, PEG-GNSs@TBO suspensions with the TBO $4 \mu\text{M}$ solution alone, in biofilm inhibition and eradication treatments and with and without laser irradiation.

The biofilm formations inhibition assays for the MRSA and *S. epidermidis* RP62A bacterial strains, showed a significant difference between the samples that were exposed or unexposed to laser irradiation (Fig. 6A–D). Biofilm formation was almost completely inhibited, for both bacterial strains, after treatment with either the nanoconjugates or the TBO solution and laser exposure, in comparison the untreated bacterial samples. On the other hand, the samples that were treated but not exposed to laser irradiation showed marked biofilm formation, approximately 75–90% more biofilm mass in comparison to that observed in untreated samples.

In dark conditions, the PEG-GNSs@TBO samples were $\sim 10\%$ more effective in reducing biofilm formation than TBO alone, against both strains (Fig. 6B and D). The PEG-GNPs@TBO treatment, however, only outperformed (with a 10% increase in biofilm inhibition) TBO alone against *S. epidermidis* RP62A cultures (Fig. 6C). We performed the same tests using only PEG-GNPs and PEG-GNSs with and without laser irradiation as a control experiment (Fig. S5†). In the case of PEG-GNPs, there was a little difference in the percentage of biofilm formations between samples whether they were treated in dark conditions or were irradiated (Fig. S5A†). With the PEG-GNSs, on the other hand, there was a much more noticeable difference between samples that had undergone laser irradiation and those that had not (Fig. S5B†). We attribute this increased effectiveness in reducing biofilm formations to the laser irradiation absorbed by PEG-GNSs which, in turn, may cause an antibacterial photothermal effect.^{42,47,56} We speculate that this induced photothermal effect may further stimulate the release of the silver ions from the GNSs lattice,⁴² increasing again the antibacterial effect.⁵³

Based on these results, we chose to further support our data by performing a SEM qualitative assessment. Given that biofilm formation was almost completely inhibited with the treatments after exposure to laser, we carried out a SEM analysis to visualize the effect of PEG-GNSs@TBO as a representative treatment. As reported in (Fig. 6E–H), the images before and after laser irradiation supported the CV biofilm inhibition assay data (Fig. 6B and D), *i.e.*, the practical absence of biofilm formation after laser exposure and in presence of PEG-GNSs@TBO. The samples that were grown, in presence of PEG-GNSs@TBO but without exposure to laser, on the other hand, showed a normal biofilm growth (Fig. 6E and G). This would roughly be similar to the levels of biofilm development in the absence of treatment (Fig. S7A and D†).

The aPDI effect of TBO has been well documented.^{27,28,30,57} Once irradiated with a light source of an appropriate wavelength (600–660 nm)⁵⁸ the aPDI has the potential to generate a cytotoxic ROS that is able to eradicate bacterial cells. We used a CW laser diode of 638 nm with an output power of $\sim 0.2 \text{ W cm}^{-2}$ for 15 minutes in all of our aPDI assays. The laser wavelength was chosen to be close to the TBO absorption maxima, at 634 nm within the used concentration, to ensure a high quantum yield of ROS generation.³¹ It is worth noting here that the power and wavelength of the laser fall within the maximum permissible



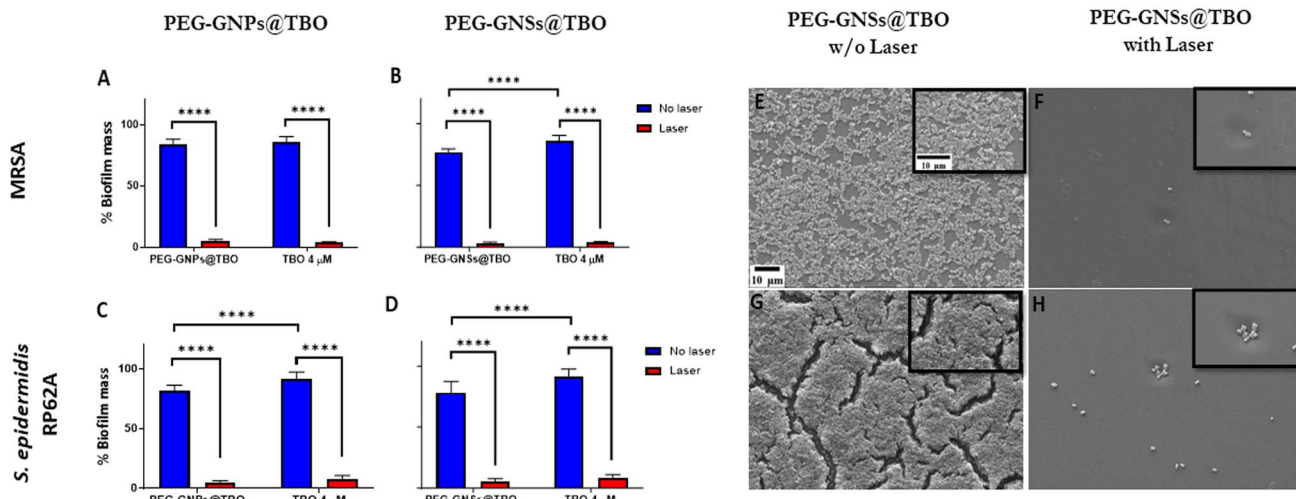


Fig. 6 aPDI effects of PEG-GNPs@TBO and PEG-GNSs@TBO on *Staphylococcal* biofilm formations. To evaluate the aPDI effects exerted by PEG-GNPs@TBO, PEG-GNSs@TBO or TBO alone on biofilm formations by MRSA [A and B] and *S. epidermidis* RP62A [C and D] planktonic cultures, CV assay was performed. Percentage of biofilm mass formations was calculated as indicated in Materials and methods in Section 2.2.6.1. Data were expressed as mean \pm standard deviations ($n = 3$). Test groups were compared using one-way variance analysis (ANOVA), followed by Bonferroni post hoc, for multiple comparisons where: *** $p < 0.0001$. SEM images of MRSA [E and F] and *S. epidermidis* RP62A [G and H] planktonic cultures upon PEG-GNSs@TBO treatment in dark conditions and with laser exposure as indicated. SEM images [within black frames] represent specific sections from same corresponding images at a larger magnification.

exposure (MPE) limits for skin, as stated by the American National Standard for Safe Use of Lasers.⁵⁹ There was a significant biofilm formation inhibition with PEG-GNPs@TBO and PEG-GNSs@TBO, along with TBO alone, nonetheless the nanoconjugates did not outperform the TBO alone in inhibiting biofilm formation. The results did reveal, though that adsorption of TBO onto both the PEG-GNPs@TBO and PEG-GNSs@TBO suspensions did not negatively impact its aPDI effects.

3.3 aPDI effects on preformed biofilms by treatment with PEG-GNPs@TBO or PEG-GNSs@TBO

The effect of both the TBO unconjugated PEG-GNPs and PEG-GNSs was evaluated (Fig. 7) prior to the evaluation of the aPDI

exerted by PEG-GNPs@TBO and PEG-GNSs@TBO on preformed biofilms against both bacterial strains (Fig. 8).

PEG-GNSs and PEG-GNPs, at different concentrations, were assessed for their intrinsic antibacterial activity against 24 hour preformed biofilms of MRSA and *S. epidermidis* RP62A cultures (Fig. 7). This was to check for the innate antibacterial effect of PEG-GNPs or PEG-GNSs suspensions, *i.e.*, their ability to decrease the viable count of bacterial cells present within the biofilms.

For PEG-GNSs, a slight decrease in bacterial viability was measured with a plateau effect reached when incremental doses of PEG-GNSs were used (Fig. 7B). A similar biofilm viable count (plateau response) was measured for biofilm cultures of the

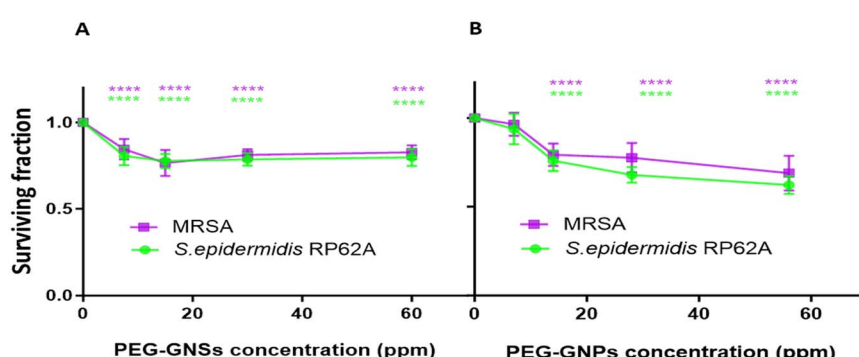


Fig. 7 Dose-dependent effects of PEG-GNPs and PEG-GNSs on the bacterial viability of preformed *Staphylococcal* biofilms. To evaluate the intrinsic dose-dependent effects of PEG-GNPs [A] and PEG-GNSs [B] on the bacterial cell viability of 24 hour preformed biofilms of MRSA and *S. epidermidis* RP62A, an MTT assay was performed. PEG-GNSs and PEG-GNPs were incubated with the preformed biofilms for 24 hours at 37 °C prior to conducting the MTT assay. Surviving fraction was calculated as indicated in Materials and methods in Section 2.2.6.1. Data were expressed as mean \pm standard deviations ($n = 3$). Test groups were compared to the untreated samples using one-way variance analysis (ANOVA), followed by Bonferroni post hoc, for multiple comparisons where: *** $p < 0.0001$.

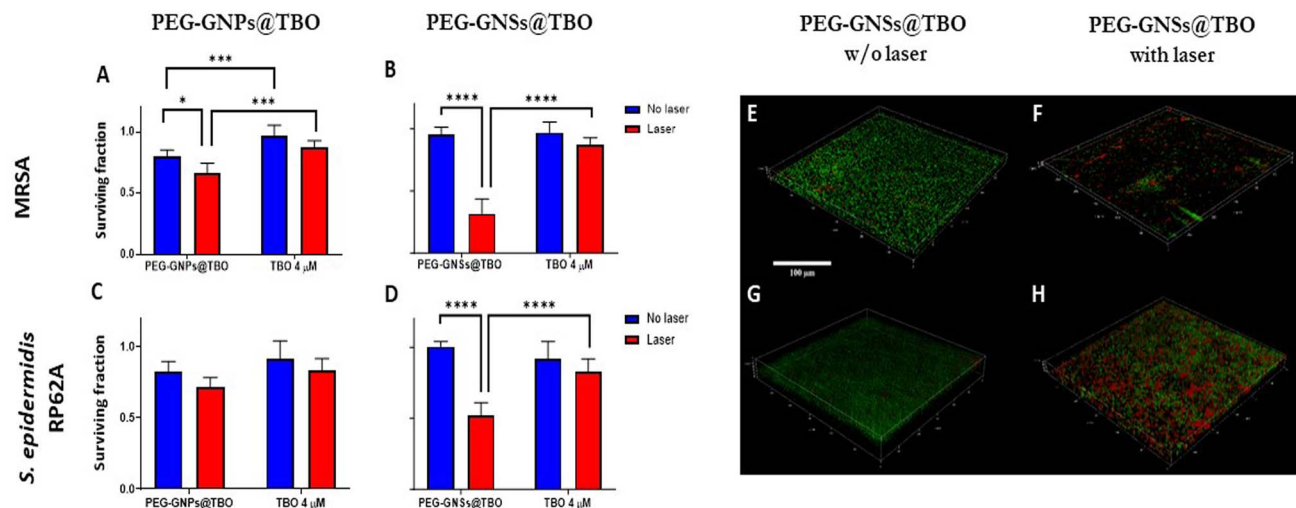


Fig. 8 aPDI effects of PEG-GNPs@TBO or PEG-GNSs@TBO on the bacterial viability of preformed *Staphylococcal* biofilms. To evaluate the aPDI effect on the bacterial viability of 24 hour preformed biofilms of MRSA [A and B] and *S. epidermidis* RP62A [C and D] upon treatments with PEG-GNPs@TBO, PEG-GNSs@TBO or TBO alone, an MTT assay was performed. Surviving fraction was calculated as indicated in Materials and methods in Section 2.2.6.1. Data were expressed as mean \pm standard deviations ($n = 3$). Test groups were compared using one-way variance analysis (ANOVA), followed by Bonferroni post hoc, for multiple comparisons where: * $p < 0.05$, *** $p < 0.001$, **** $p < 0.0001$. Live/dead 3D CLSM projections of MRSA [E and F] and *S. epidermidis* RP62A [G and H] preformed biofilms upon treatment with PEG-GNSs@TBO in dark conditions and with laser exposure as indicated. Live cells were stained in green by SYTO 9 and dead cells stained in red by propidium iodide PI. Scale bar: 100 μ m.

same bacterial strains, when tested against a range of different TBO concentrations (Fig. S6A†). In the case, alternatively, of PEG-GNPs the reduction in bacterial viability was correlated with incremental doses, with a slightly more pronounced antibacterial effect at higher doses (Fig. 7A). This result agrees with previous studies of the relationship between AuNPs size and their biofilm eradication efficacy^{60,61} where smaller AuNPs were shown to be more capable of eliminating bacterial cells present in mature biofilms due to their increased ability to penetrate cellular membrane barriers. The same concentrations of PEG-GNPs@TBO and PEG-GNSs@TBO that were used in the biofilm formations inhibition assays (Section 3.2) were assessed again to understand their effect on laser treatment against 24 hour preformed biofilm cultures of MRSA and *S. epidermidis* RP62A.

PEG-GNSs@TBO had superior aPDI effects against the pre-formed biofilms of both bacterial strains. The treatment reduced bacterial viability of MRSA and *S. epidermidis* RP62A biofilms by 75% and 50%, respectively, in comparison to a 12% and 17% reduction with TBO alone for the same bacterial strains (Fig. 8B and D). It is interesting to note that the PEG-GNSs@TBO samples were able to reduce bacterial viability only slightly, without laser irradiation. This suggests that this nanoconjugate system would be suitable as an on-demand antibacterial effect. The antibacterial activity of PEG-GNPs@TBO, however, was lower and only slightly more effective than TBO alone (Fig. 8A and C). The bacterial viability of MRSA and *S. epidermidis* RP62A biofilm cultures were reduced by around 35% and 30%, respectively, upon treatment with PEG-GNPs@TBO and laser exposure. This compares to reduction rates of just 13% and 17% with the TBO solution alone for

the same bacterial strains (Fig. 8B and D). Bacterial viability was not reduced significantly in samples that were not exposed to laser irradiation. Samples treated in dark conditions by PEG-GNPs@TBO showed the highest reduction, followed by TBO alone and PEG-GNSs@TBO in the same corresponding order (Fig. 8). It is worth noting that for both bacterial strains, we tested the effect of laser alone, TBO unconjugated PEG-GNPs and PEG-GNSs suspensions with laser exposure as an experimental control to check for their antibacterial effects in biofilm inhibition and eradication treatments. With laser treatments alone, there were virtually no detected differences from the untreated bacterial samples in both biofilm inhibition and eradication treatments (Fig. S7-S10†), whereas the antibacterial effects in biofilm eradication treatments of the TBO unconjugated PEG-GNPs and PEG-GNSs suspensions were almost equivalent to those without laser exposure (Fig. S5C and D†). For comparative purposes, we also investigated the antibacterial effect of a relatively high concentration of TBO (40 μ M) against preformed biofilms of the same bacterial strains (Fig. S6B†). A reduction of nearly 30% in bacterial viability was measured for both strains after 15 minutes of laser irradiation. This result clearly demonstrates the superior antibacterial effects achieved via the adsorption of TBO to GNSs, as a treatment with a ten times more concentrated solution of TBO (40 μ M), did not result in the same extent of reduction in bacterial viability as that attained by the aPDI treatment of PEG-GNSs@TBO. Given the promising aPDI data with the PEG-GNSs@TBO treatments, we decided to conduct a LIVE/DEAD® assay utilizing a BacLight bacterial viability kit L7012 and CLSM microscopy to check for the bacterial viability and the morphological changes following preformed biofilm treatment with PEG-GNSs@TBO, with and



without laser exposure (Fig. 8E–H). Both treated biofilms (Fig. 8E and G), showed predominantly green-fluorescing, viable, cells after treatment with PEG-GNSs@TBO without laser irradiation. This agrees with the results of the antibacterial MTT assays (Fig. 8A and C). Increased levels of cellular death, however and as demonstrated by a higher percentage of red-fluorescing cells, were observed in biofilms treated with PEG-GNSs@TBO and laser irradiation (Fig. 8F and H), along with morphological changes. To further support our data, we also performed a SEM imaging analysis to visualize the antibacterial effects of the treatments on the preformed biofilms (Fig. 9A–D). SEM images demonstrated a clear difference in biofilm integrity for samples that were (Fig. 9B and D) and were not (Fig. 9A and C) exposed to laser. Bacterial cell clusters within biofilms that were treated with PEG-GNSs@TBO and exposed to laser were much more fragmented than those that had not been exposed to laser. Using the same samples, we conducted also atomic force microscopy imaging (AFM) to further examine the biofilm surface morphology before and after treatments. The uniform and smooth biofilm surface morphology in dark conditions is confirmed by AFM images on the micro-meter scale (Fig. 9E and G). On the other hand, after laser treatment, AFM images clearly demonstrated a detrimental effect on biofilm integrity (Fig. 9F and H). These images show that PEG-GNSs@TBO aPDI treatment can also facilitate and enhance the diffusion of other antimicrobials into biofilms. This may consequently lead to better therapeutic outcomes as antimicrobials gain access to deeper bacterial cell layers.⁶² Our quantitative and qualitative assays results confirmed that the antibacterial effects of PEG-GNSs@TBO were attributed to the photodynamic activation of the conjugated TBO. As a result, we assessed laser induced ROS generation with the fluorescent probe CellROX™ Deep Red.

This cell-permeant dye is non-fluorescent while in a reduced state but exhibits bright red fluorescence upon oxidation by ROS. Previous studies reported the successful use of the same probe for detecting oxidative stress in bacteria.^{63,64} Our CLSM images revealed a clear difference between the samples that were treated in dark conditions, and those which were laser irradiated ($\sim 0.2 \text{ W cm}^{-2}$ at 638 nm for 15 min). Following treatment with PEG-GNSs@TBO, but without laser irradiation, red fluorescence surface levels were barely detectable (Fig. 10A and C). In the case of bacterial biofilms that were treated with PEG-GNSs@TBO and exposed to laser, however, numerous bright red spots were clearly observed in different locations (Fig. 10B and D). This confirms the laser induced ROS production by PEG-GNSs@TBO ROS production. Using a dedicated image processing software (ImageJ) we managed to quantify the ROS production for both bacterial samples after treatment with and without laser irradiation (Fig. 10E and F). Several previous studies^{39,65,66} have demonstrated that during the photodynamic activation of a PS, the generation of ROS and, in particular, singlet oxygen species (${}^1\text{O}_2$) can be significantly elevated by the localized surface plasmon resonance of gold nanoparticles. It has been argued that the LSPR of Au nanoparticles enhances photocurrent and leads, once activated by a suitable light source, to an energy transfer to the PS. This, gained, energy is transferred into elevated ROS formation.⁶⁶ Khan *et al.*⁶⁷ have demonstrated enhanced aPDI effects in methylene blue MB, a PS which is close in structure to TBO, when conjugated with Concanavalin-A (ConA) directed dextran capped gold nanospheres $\sim 36 \text{ nm}$ in diameter. This was attributed to the AuNPs plasmon field that excited MB molecules located in the proximity of the nanoparticles, when they were subjected to a suitable light source.⁶⁸ These studies

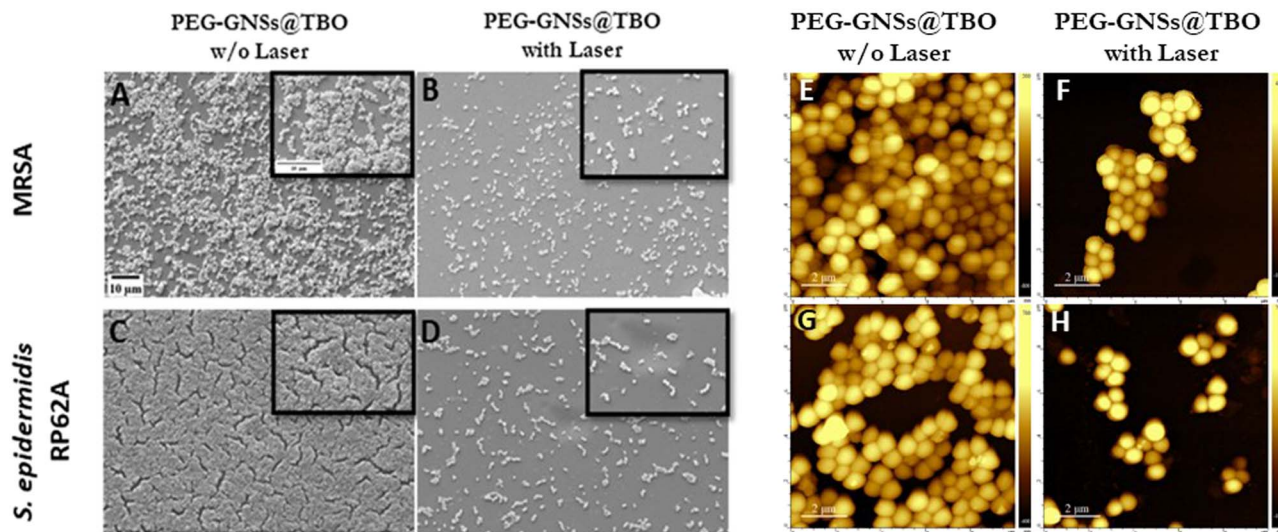


Fig. 9 Bacterial biofilms images after aPDI effect of PEG-GNSs@TBO. SEM images of MRSA [A and B] and *S. epidermidis* RP62A [C and D] preformed biofilms upon treatment with PEG-GNSs@TBO in dark conditions and with laser exposure as indicated (scale bar: $10 \mu\text{m}$). SEM images [within black frames] represent specific sections from same corresponding images at a larger magnification. Tapping mode 2D AFM topographical images for the same samples studied: MRSA [E and F] and *S. epidermidis* RP62A [G and H] preformed biofilms upon PEG-GNSs@TBO treatment both in dark conditions and with laser exposure, respectively (scale bar: $2 \mu\text{m}$).



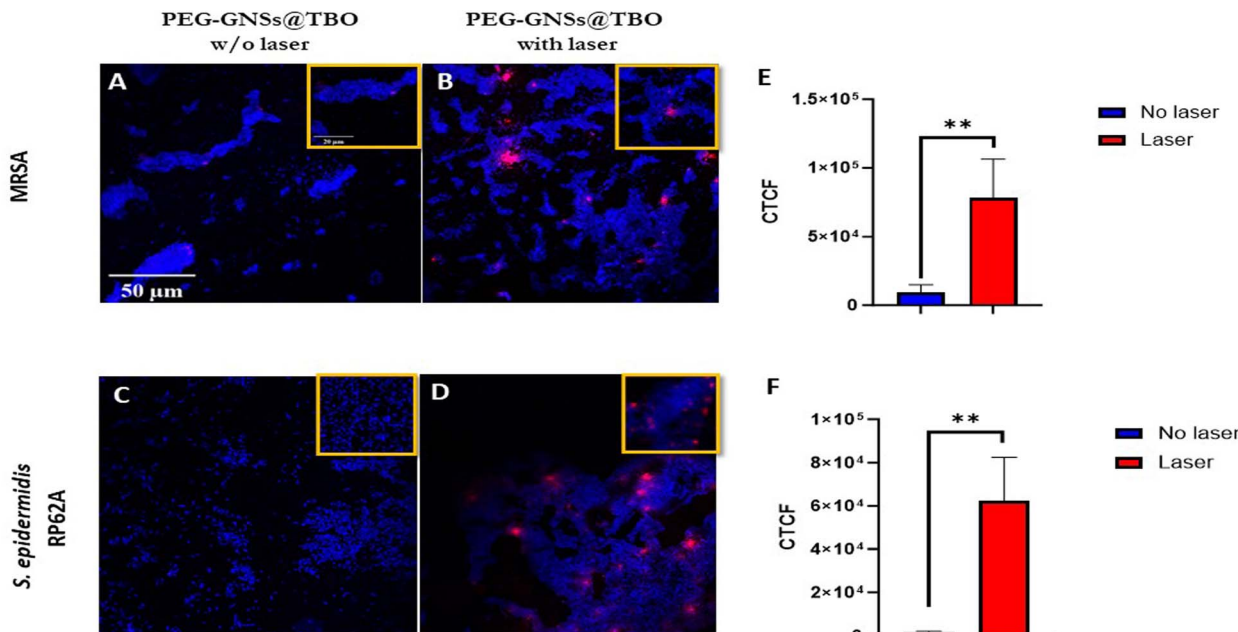


Fig. 10 Fluorescent detection of ROS formation after treatment with PEG-GNSs@TBO. CellROX® Deep Red/Hoechst 33342 stained CLSM images for the ROS detection on MRSA [A and B] and *S. epidermidis* RP62A [C and D] preformed biofilms upon treatment with PEG-GNSs@TBO in dark conditions and with laser exposure as indicated. Scale bar: 50 μ m. CLSM images [within the yellow frames] represent a selected section from the same corresponding images at a larger magnification. Mean of fluorescence intensity [E and F], expressed as CTCF (corrected total cell fluorescence), determined for MRSA [E] and *S. epidermidis* RP62A [F] after laser exposure. Data were expressed as mean \pm standard deviations ($n = 3$). Test groups were compared using Student's *t*-test where: ** $p < 0.01$.

support the position of this paper, *i.e.* the increased efficacy, in terms of aPDI levels, of the TBO conjugated with PEG-GNSs@TBO when compared with TBO alone. Moreover, Khaing Oo *et al.*³⁹ reported that enhanced ROS generation, in conjugating the PS protoporphyrin IX on the surface of GNPs, is size-dependent. Functionalized GNPs with a 106 nm diameter presented an enhancement ratio which was 11 times greatest than that of 19 nm samples and of 3.5 times those of 66 nm. The larger the GNPs, the stronger the effect. This finding agrees with our results and may help to explain the enhanced aPDI effects of PEG-GNSs@TBO over the smaller PEG-GNPs@TBO. Moreover, the well-known ability of GNPs to enhance the electric field around their sharp edges and tips⁶⁹ may also contribute to an increase in ROS generation in irradiated PEG-GNSs@TBO. Finally, another factor that may have contributed to the enhanced antibacterial activity of our nanoconjugates is the presence of the cationic TBO on the outer polymer surface. As reported by previous literature^{27,29,30,70} this should have aided the electrostatic interaction between the nanoconjugates with the negatively charged bacterial cell surface²⁶ and extracellular polymer substances (EPS) of bacterial biofilms.⁷¹ Another aspect that is important to discuss is the safety of our nanoconjugates as a potential candidate therapeutic for superficial biofilm infections, such as those found in chronic infected wounds. Moderate to high ROS production from exogenous factors is known to contribute to oncogenesis, and indirectly may cause cell mutations leading eventually to cell death.⁷² Since our nanoconjugates are targeted towards bacterial infections

present on the skin, this may justify the possible damage caused by ROS production, based on two facts: first, skin is a regenerative organ, meaning that possible damage arising from exogenous ROS production won't be irreversible and eventually damaged skin tissue will be replaced by healthy intact one.⁷³ Second, is that our nanoconjugates may offer an alternative therapeutic to infected chronic wounds, including systemic antibiotic treatments or even some last-resort treatments notably amputations. From a benefit-risk ratio point of view, avoiding the administration of systemic antibiotics with all of its associated side effects,⁷⁴ or preventing an amputation surgery outweighs the possible side effects arising from ROS production to nearby skin tissue.

4. Conclusions

This paper sheds light on the antibacterial potential of gold nanoparticles as carriers for photosensitizers and indicates how this synergism can be harnessed to provide efficient anti-biofilm therapeutics in an era where pathogenic biofilms represent a major and global concern for health-care systems.

We compared the intrinsic antibacterial activity of two kinds of PEGylated gold nanoparticles, PEG-GNPs and PEG-GNSs, and their aPDI effects upon functionalization with TBO. We demonstrated that the antibacterial potential of a PS like TBO can be significantly enhanced by adsorption onto a metallic nanoplateform like gold nanoparticles.

Our findings revealed that differences in NP shapes and sizes impact their intrinsic antibacterial efficacies and their aPDI



effects when used as a carrier for the PS TBO. Although both nanoconjugates and TBO solutions exhibited remarkable aPDI effects in inhibiting biofilm formation, only the PEG-GNss@TBO treatment, in terms of aPDI effects, was able to notably reduce bacterial viability on 24 hour preformed biofilms. CLSM and SEM images also demonstrated the ability of PEG-GNss@TBO aPDI's to disrupt biofilm integrity. This effect can be repurposed by deploying this treatment to increase the effectiveness, *via* enhanced levels of biofilm diffusion, of other antimicrobial treatments.

Our results were achieved using a laser within the maximum permissible skin exposure levels. This paves the way for optimizing and employing our findings in future studies for treating clinically related biofilm infections. We firmly believe that there is huge potential to develop other synergistic photodynamic nanoplatforms, as novel and efficacious antibiofilm therapeutics.

Author contributions

Conceptualization, M. O., L. V.; data curation, M. O., L. D. V., E. R., L. D.; formal analysis, M. O., L. D. V., E. R., G. B., L. D., M. P.; funding acquisition, L. V.; project administration, M. O., L. V.; resources, L. V., P. P., G. B., M. P., P. M.; software, M. O., L. D. V., L. D., E. R., G. B., M. P., L. D.; visualization M. O., L. V.; methodology, M. O., L. D. V., E. R., L. V., P. P; validation, M. O., L. V., P. M., P. P.; investigation, M. O.; writing—original draft, M. O.; writing – review & editing, L. V., P. P., P. M.; supervision, L. V., P. P.; all authors have read and agreed to the published version of the manuscript.

Conflicts of interest

There are no conflicts to declare.

Acknowledgements

L. V. acknowledge the grant of the Italian Ministry of University and Research (MUR) to the Department of Molecular Medicine of the University of Pavia under the initiative “Dipartimenti di Eccellenza (2018–2022 and 2023–2027)”. L. D. V. thanks Ministero dell’Università e della Ricerca (MUR) for the PRIN (2017EKCS35) grant “SUNSET – SUPramolecular and Nanostructured Systems for the analysis of Emerging pollutants through optical Transduction”. L. D. V., P. P. and L. D. acknowledge support to the Department of Chemistry of the University of Pavia from the Ministero dell’Università e della Ricerca (MUR) through the program “Dipartimenti di Eccellenza (2023–2027)”. Special thanks go to the Italian Agency for Development and Cooperation (AICS), the Center of International Cooperation and Development (CICOPS) at the University of Pavia, and the Partnership for Knowledge (PFK) initiative for offering a PhD scholarship in Translational Medicine to M. O. This work is part of the PhD thesis of M. O. We are grateful to P. Vaghi (Centro Grandi Strumenti (https://cgs.unipv.it/eng/?page_id=84), University of Pavia, Pavia, Italy) for her technical assistance in the CLSM observations. A special thanks to Scott

Burgess (University of Pavia, Pavia, Italy) for correcting the English in the manuscript.

References

- P. R. Chadwick, Revised UK guidelines for the control of methicillin-resistant *Staphylococcus aureus* in hospitals, *Int. J. Antimicrob. Agents*, 1999, **11**(2), 89–91, DOI: [10.1016/S0924-8579\(98\)00103-4](https://doi.org/10.1016/S0924-8579(98)00103-4).
- K. Honma, Y. Tawara and K. Okuda, Detection of methicillin-resistant *staphylococcus aureus* in human saliva and on denture surfaces, *Bull. Tokyo Dent. Coll.*, 1994, **35**(4), 217–220.
- R. H. Deurenberg and E. E. Stobberingh, The evolution of *Staphylococcus aureus*, *Infect., Genet. Evol.*, 2008, **8**(6), 747–763, DOI: [10.1016/J.MEEGID.2008.07.007](https://doi.org/10.1016/J.MEEGID.2008.07.007).
- P. O. Lewis, E. L. Heil, K. L. Covert and D. B. Cluck, Treatment strategies for persistent methicillin-resistant *Staphylococcus aureus* bacteraemia, *J. Clin. Pharm. Ther.*, 2018, **43**(5), 614–625, DOI: [10.1111/JCPT.12743](https://doi.org/10.1111/JCPT.12743).
- J. Rolo, P. Worning, J. Boye Nielsen, *et al.*, Evidence for the evolutionary steps leading to *mecA*-mediated β -lactam resistance in staphylococci, *PLoS Genet.*, 2017, **13**(4), e1006674, DOI: [10.1371/JOURNAL.PGEN.1006674](https://doi.org/10.1371/JOURNAL.PGEN.1006674).
- I. d. P. Ribeiro, J. G. Pinto, B. M. N. Souza, A. G. Miñán and J. Ferreira-Strixino, Antimicrobial photodynamic therapy with curcumin on methicillin-resistant *Staphylococcus aureus* biofilm, *Photodiagn. Photodyn. Ther.*, 2022, **37**, 102729, DOI: [10.1016/J.PDPDT.2022.102729](https://doi.org/10.1016/J.PDPDT.2022.102729).
- M. Otto, *Staphylococcus epidermidis* – the “accidental” pathogen, *Nat. Rev. Microbiol.*, 2009, **7**(8), 555, DOI: [10.1038/NRMICRO2182](https://doi.org/10.1038/NRMICRO2182).
- N. Haque, M. S. Bari, N. Haque, *et al.*, Methicillin resistant *Staphylococcus epidermidis*, *Mymensingh Med. J.*, 2011, **20**(2), 326–331, <https://pubmed.ncbi.nlm.nih.gov/21522111/>, accessed December 20, 2022.
- R. M. Donlan, Biofilms: Microbial Life on Surfaces - Volume 8, Number 9—September 2002 - Emerging Infectious Diseases journal - CDC, *Emerging Infect. Dis.*, 2002, **8**(9), 881–890, DOI: [10.3201/EID0809.020063](https://doi.org/10.3201/EID0809.020063).
- Y. H. E. Mohammed, H. M. Manukumar, K. P. Rakesh, C. S. Karthik, P. Mallu and H. L. Qin, Vision for medicine: *Staphylococcus aureus* biofilm war and unlocking key's for anti-biofilm drug development, *Microb. Pathog.*, 2018, **123**, 339–347, DOI: [10.1016/J.MICPATH.2018.07.002](https://doi.org/10.1016/J.MICPATH.2018.07.002).
- D. E. Moormeier and K. W. Bayles, *Staphylococcus aureus* biofilm: a complex developmental organism, *Mol. Microbiol.*, 2017, **104**(3), 365–376, DOI: [10.1111/MMI.13634](https://doi.org/10.1111/MMI.13634).
- A. E. Paharik and A. R. Horswill, The staphylococcal biofilm: Adhesins, regulation, and host response, *Virulence Mech. Bact. Pathog.*, 2016, 529–566, DOI: [10.1128/9781555819286.CH19](https://doi.org/10.1128/9781555819286.CH19).
- Y. Liu, L. Shi, L. Su, *et al.*, Nanotechnology-based antimicrobials and delivery systems for biofilm-infection control, *Chem. Soc. Rev.*, 2019, **48**(2), 428–446, DOI: [10.1039/C7CS00807D](https://doi.org/10.1039/C7CS00807D).



14 Z. Khatoon, C. D. McTiernan, E. J. Suuronen, T. F. Mah and E. I. Alarcon, Bacterial biofilm formation on implantable devices and approaches to its treatment and prevention, *Helijon*, 2018, 4(12), 1067, DOI: [10.1016/J.HELION.2018.E01067](#).

15 E. P. Magennis, A. L. Hook, P. Williams and M. R. Alexander, Making silicone rubber highly resistant to bacterial attachment using thiol-ene grafting, *ACS Appl. Mater. Interfaces*, 2016, 8(45), 30780–30787, DOI: [10.1021/ACSAM.6B10986/SUPPL_FILE/AM6B10986_SI_001.PDF](#).

16 B. Geng, S. Xu, P. Li, *et al.*, Platinum Crosslinked Carbon Dot@TiO₂-x p-n Junctions for Relapse-Free Sonodynamic Tumor Eradication via High-Yield ROS and GSH Depletion, *Small*, 2022, 18(6), 2103528, DOI: [10.1002/SMIL.202103528](#).

17 B. Geng, J. Hu, Y. Li, *et al.*, Near-infrared phosphorescent carbon dots for sonodynamic precision tumor therapy, *Nat. Commun.*, 2022, 13(1), 5735, DOI: [10.1038/S41467-022-33474-8](#).

18 B. Geng, Y. Li, J. Hu, *et al.*, Graphitic-N-doped graphene quantum dots for photothermal eradication of multidrug-resistant bacteria in the second near-infrared window, *J. Mater. Chem. B*, 2022, 10(17), 3357–3365, DOI: [10.1039/D2TB00192F](#).

19 X. Zhao, R. Shen, L. Bao, C. Wang and H. Yuan, Chitosan derived glycolipid nanoparticles for magnetic resonance imaging guided photodynamic therapy of cancer, *Carbohydr. Polym.*, 2020, 245, 116509, DOI: [10.1016/J.CARBPOL.2020.116509](#).

20 L. Song, L. Sun, J. Zhao, *et al.*, Synergistic Superhydrophobic and Photodynamic Cotton Textiles with Remarkable Antibacterial Activities, *ACS Appl. Bio Mater.*, 2019, 2(7), 2756–2765, DOI: [10.1021/ACSABM.9B00149](#).

21 K. Konopka and T. Goslinski, Photodynamic therapy in dentistry, *J. Dent. Res.*, 2007, 86(8), 694–707, DOI: [10.1177/154405910708600803](#).

22 E. Buytaert, M. Dewaele and P. Agostinis, Molecular effectors of multiple cell death pathways initiated by photodynamic therapy, *Biochim. Biophys. Acta, Rev. Cancer*, 2007, 1776(1), 86–107, DOI: [10.1016/J.BBCCAN.2007.07.001](#).

23 Z. Zou, H. Chang, H. Li and S. Wang, Induction of reactive oxygen species: an emerging approach for cancer therapy, *Apoptosis*, 2017, 22(11), 1321–1335, DOI: [10.1007/S10495-017-1424-9](#).

24 D. M. A. Vera, M. H. Haynes, A. R. Ball, *et al.*, Strategies to potentiate antimicrobial photoactivation by overcoming resistant phenotypes, *Photochem. Photobiol.*, 2012, 88(3), 499–511, DOI: [10.1111/J.1751-1097.2012.01087.X](#).

25 T. Maisch, Resistance in antimicrobial photodynamic inactivation of bacteria, *Photochem. Photobiol. Sci.*, 2015, 14(8), 1518–1526, DOI: [10.1039/C5PP00037H](#).

26 M. N. Usacheva, M. C. Teichert and M. A. Biel, The role of the methylene blue and toluidine blue monomers and dimers in the photoactivation of bacteria, *J. Photochem. Photobiol. B*, 2003, 71(1–3), 87–98, DOI: [10.1016/J.JPHOTOBIOL.2003.06.002](#).

27 M. N. Usacheva, M. C. Teichert and M. A. Biel, Comparison of the methylene blue and toluidine blue photobactericidal efficacy against gram-positive and gram-negative microorganisms, *Lasers Surg. Med.*, 2001, 29(2), 165–173, DOI: [10.1002/LSM.1105](#).

28 L. Misba, H. Abdulrahman and A. U. Khan, Photodynamic efficacy of toluidine blue O against mono species and dual species bacterial biofilm, *Photodiagn. Photodyn. Ther.*, 2019, 26, 383–388, DOI: [10.1016/J.PDPDT.2019.05.001](#).

29 R. Wiench, D. Skaba, J. Matys and K. Grzech-Leśniak, Efficacy of Toluidine Blue–Mediated Antimicrobial Photodynamic Therapy on *Candida* spp. A Systematic Review, *Antibiotics*, 2021, 10(4), 349, DOI: [10.3390/ANTIBIOTICS10040349](#).

30 M. Sharma, L. Visai, F. Bragheri, I. Cristiani, P. K. Gupta and P. Speziale, Toluidine blue-mediated photodynamic effects on staphylococcal biofilms, *Antimicrob. Agents Chemother.*, 2008, 52(1), 299–305, DOI: [10.1128/AAC.00988-07](#).

31 F. Akhtar, A. U. Khan, B. Qazi, *et al.*, A nano phototheranostic approach of toluidine blue conjugated gold silver core shells mediated photodynamic therapy to treat diabetic foot ulcer, *Sci. Rep.*, 2021, 11(1), 1–19, DOI: [10.1038/s41598-021-04008-x](#).

32 M. I. Mohammed, I. S. Yahia and G. F. Salem, Design of a smart optical sensor employing Toluidine Blue dye as an effective laser optical limiter integrated into (PVA) composite films: Electrical conductivity and dielectric characteristics improvement, *Opt. Laser Technol.*, 2022, 156, 108629, DOI: [10.1016/J.OPTLASTEC.2022.108629](#).

33 U. Wnorowska, K. Fiedoruk, E. Piktel, *et al.*, Nanoantibiotics containing membrane-active human cathelicidin LL-37 or synthetic ceragenins attached to the surface of magnetic nanoparticles as novel and innovative therapeutic tools: Current status and potential future applications, *J. Nanobiotechnol.*, 2020, 18(1), 1–18, DOI: [10.1186/S12951-019-0566-Z/FIGURES/3](#).

34 A. M. Alkilany and C. J. Murphy, Toxicity and cellular uptake of gold nanoparticles: What we have learned so far?, *J. Nanopart. Res.*, 2010, 12, 2313–2333, DOI: [10.1007/s11051-010-9911-8](#).

35 S. Shamaila, N. Zafar, S. Riaz, R. Sharif, J. Nazir and S. Naseem, Gold Nanoparticles: An Efficient Antimicrobial Agent against Enteric Bacterial Human Pathogen, *Nanomater*, 2016, 6(4), 71, DOI: [10.3390/NANO6040071](#).

36 M. M. Mohamed, S. A. Fouad, H. A. Elshoky, G. M. Mohammed and T. A. Salaheldin, Antibacterial effect of gold nanoparticles against *Corynebacterium pseudotuberculosis*, *Int. J. Vet. Sci. Med.*, 2017, 5(1), 23–29, DOI: [10.1016/j.ijvsm.2017.02.003](#).

37 L. M. Rossi, P. R. Silva, L. L. R. Vono, A. U. Fernandes, D. B. Tada and M. S. Baptista, Protoporphyrin IX nanoparticle carrier: Preparation, optical properties and singlet oxygen generation, *Langmuir*, 2008, 24(21), 12534–12538, DOI: [10.1021/LA800840K](#).

38 Y. Cheng, J. D. Meyers, A. M. Broome, M. E. Kenney, J. P. Basilion and C. Burda, Deep penetration of a PDT drug into tumors by noncovalent drug-gold nanoparticle conjugates, *J. Am. Chem. Soc.*, 2011, 133(8), 2583–2591, DOI: [10.1021/JA108846H](#).



39 M. K. Khaing Oo, Y. Yang, Y. Hu, M. Gomez, H. Du and H. Wang, Gold nanoparticle-enhanced and size-dependent generation of reactive oxygen species from protoporphyrin IX, *ACS Nano*, 2012, **6**(3), 1939–1947, DOI: [10.1021/NN300327C](https://doi.org/10.1021/NN300327C).

40 D. B. Tada and M. S. Baptista, Photosensitizing nanoparticles and the modulation of ROS generation, *Front. Chem.*, 2015, **3**(MAY), 33, DOI: [10.3389/FCHEM.2015.00033](https://doi.org/10.3389/FCHEM.2015.00033).

41 J. Turkevich, P. C. Stevenson and J. Hillier, A study of the nucleation and growth processes in the synthesis of colloidal gold, *Discuss. Faraday Soc.*, 1951, **11**, 55–75, DOI: [10.1039/DF9511100055](https://doi.org/10.1039/DF9511100055).

42 P. Pallavicini, S. Basile, G. Chirico, *et al.*, Monolayers of gold nanostars with two near-IR LSPRs capable of additive photothermal response, *Chem. Commun.*, 2015, **51**(65), 12928–12930, DOI: [10.1039/C5CC04144A](https://doi.org/10.1039/C5CC04144A).

43 G. D. Christensen, W. A. Simpson, J. J. Younger, *et al.*, Adherence of coagulase-negative staphylococci to plastic tissue culture plates: a quantitative model for the adherence of staphylococci to medical devices, *J. Clin. Microbiol.*, 1985, **22**(6), 996, DOI: [10.1128/JCM.22.6.996-1006.1985](https://doi.org/10.1128/JCM.22.6.996-1006.1985).

44 P. Pallavicini, C. R. Arciola, F. Bertoglio, *et al.*, Silver nanoparticles synthesized and coated with pectin: An ideal compromise for anti-bacterial and anti-biofilm action combined with wound-healing properties, *J. Colloid Interface Sci.*, 2017, **498**, 271–281, DOI: [10.1016/J.JCIS.2017.03.062](https://doi.org/10.1016/J.JCIS.2017.03.062).

45 D. Keith Roper, K. R. Berry, A. G. Russell, P. A. Blake and D. Keith Roper, Gold nanoparticles reduced in situ and dispersed in polymer thin films: optical and thermal properties, *Nanotechnology*, 2012, **23**(37), 375703, DOI: [10.1088/0957-4484/23/37/375703](https://doi.org/10.1088/0957-4484/23/37/375703).

46 K. Rahme, M. T. Nolan, T. Doody, *et al.*, Highly stable PEGylated gold nanoparticles in water: applications in biology and catalysis, *RSC Adv.*, 2013, **3**(43), 21016–21024, DOI: [10.1039/C3RA41873A](https://doi.org/10.1039/C3RA41873A).

47 P. Grisoli, L. De Vita, C. Milanese, *et al.*, Pva films with mixed silver nanoparticles and gold nanostars for intrinsic and photothermal antibacterial action, *Nanomaterials*, 2021, **11**(6), 1387, DOI: [10.3390/nano11061387](https://doi.org/10.3390/nano11061387).

48 Y. Zhang, T. P. Shareena Dasari, H. Deng and H. Yu, Antimicrobial Activity of Gold Nanoparticles and Ionic Gold, *J. Environ. Sci. Health, Part C: Environ. Carcinog. Ecotoxicol. Rev.*, 2015, **33**(3), 286–327, DOI: [10.1080/10590501.2015.1055161](https://doi.org/10.1080/10590501.2015.1055161).

49 E. A. Ortiz-Benítez, N. Velázquez-Guadarrama, N. V. Durán Figueroa, H. Quezada and J. De Jesús Olivares-Trejo, Antibacterial mechanism of gold nanoparticles on: *Streptococcus pneumoniae*, *Metallomics*, 2019, **11**(7), 1265–1276, DOI: [10.1039/c9mt00084d](https://doi.org/10.1039/c9mt00084d).

50 V. Ivanovic, D. Popovic, S. Petrovic, *et al.*, Unraveling the Antibiofilm Activity of a New Nanogold Resin for Dentures and Epithesis, *Pharmaceutics*, 2022, **14**(7), 1513, DOI: [10.3390/PHARMACEUTICS14071513](https://doi.org/10.3390/PHARMACEUTICS14071513).

51 D. P. Linklater, V. A. Baulin, X. Le Guével, *et al.*, Antibacterial Action of Nanoparticles by Lethal Stretching of Bacterial Cell Membranes, *Adv. Mater.*, 2020, 2005679, DOI: [10.1002/adma.202005679](https://doi.org/10.1002/adma.202005679).

52 J. Penders, M. Stolzoff, D. J. Hickey, M. Andersson and T. J. Webster, Shape-dependent antibacterial effects of non-cytotoxic gold nanoparticles, *Int. J. Nanomed.*, 2017, **12**, 2457–2468, DOI: [10.2147/IJN.S124442](https://doi.org/10.2147/IJN.S124442).

53 S. Chernousova and M. Epple, Silver as Antibacterial Agent: Ion, Nanoparticle, and Metal, *Angew. Chem., Int. Ed.*, 2013, **52**(6), 1636–1653, DOI: [10.1002/ANIE.201205923](https://doi.org/10.1002/ANIE.201205923).

54 P. V. Baptista, M. P. McCusker, A. Carvalho, *et al.*, Nanostrategies to fight multidrug resistant bacteria—“A Battle of the Titans”, *Front. Microbiol.*, 2018, **9**(JUL), 1–26, DOI: [10.3389/fmicb.2018.01441](https://doi.org/10.3389/fmicb.2018.01441).

55 N. N. Mahmoud, A. M. Alkilany, E. A. Khalil and A. G. Al-Bakri, Antibacterial activity of gold nanorods against *Staphylococcus aureus* and *Propionibacterium acnes*: misinterpretations and artifacts, *Int. J. Nanomed.*, 2017, **12**, 7311–7322, DOI: [10.2147/IJN.S145531](https://doi.org/10.2147/IJN.S145531).

56 D. Rovati, B. Albini, P. Galinetto, P. Grisoli, B. Bassi, P. Pallavicini, G. Dacarro and A. Taglietti, High Stability Thiol-Coated Gold Nanostars Monolayers with Photo-Thermal Antibacterial Activity and Wettability Control, *Nanomaterials*, 2019, **9**(9), 1288, DOI: [10.3390/nano9091288](https://doi.org/10.3390/nano9091288).

57 L. Misba, S. Zaidi and A. U. Khan, A comparison of antibacterial and antibiofilm efficacy of phenothiazinium dyes between Gram positive and Gram negative bacterial biofilm, *Photodiagn. Photodyn. Ther.*, 2017, **18**, 24–33, DOI: [10.1016/J.PDPDT.2017.01.177](https://doi.org/10.1016/J.PDPDT.2017.01.177).

58 L. D’Ilario and A. Martinelli, Toluidine blue: aggregation properties and structural aspects, *Modell. Simul. Mater. Sci. Eng.*, 2006, **14**(4), 581, DOI: [10.1088/0965-0393/14/4/003](https://doi.org/10.1088/0965-0393/14/4/003).

59 Laser institute of America (LIA), *American National Standard for Safe Use of Lasers, ANSI Z136.1-2007*, 2007, Orlando, FL, USA.

60 S. K. Boda, J. Broda, F. Schiefer, *et al.*, Cytotoxicity of Ultrasmall Gold Nanoparticles on Planktonic and Biofilm Encapsulated Gram-Positive Staphylococci, *Small*, 2015, **11**(26), 3183–3193, DOI: [10.1002/SMIL.201403014](https://doi.org/10.1002/SMIL.201403014).

61 D. Ahmed, A. Anwar, A. K. Khan, A. Ahmed, M. R. Shah and N. A. Khan, Size selectivity in antibiofilm activity of 3-(diphenylphosphino)propanoic acid coated gold nanomaterials against Gram-positive *Staphylococcus aureus* and *Streptococcus mutans*, *AMB Express*, 2017, **7**(1), 1–11, DOI: [10.1186/S13568-017-0515-X/FIGURES/7](https://doi.org/10.1186/S13568-017-0515-X/FIGURES/7).

62 E. Teirlinck, S. K. Samal, T. Coenye and K. Braeckmans, Penetrating the Bacterial Biofilm: Challenges for Antimicrobial Treatment, *Functionalized Nanomaterials for the Management of Microbial Infection: A Strategy to Address Microbial Drug Resistance*, 2017, pp. 49–76, DOI: [10.1016/B978-0-323-41625-2.00003-X](https://doi.org/10.1016/B978-0-323-41625-2.00003-X).

63 D. Manoil and S. Bouillaguet, Oxidative Stress in Bacteria Measured by Flow Cytometry, *Adv. Biotechnol. Microbiol.*, 2018, **8**(1), 555726, DOI: [10.19080/AIBM.2018.08.555726](https://doi.org/10.19080/AIBM.2018.08.555726).

64 N. Raatschen, M. Wenzel, L. I. Ole Leichert, P. Düchting, U. Krämer and J. Elisabeth Bandow, Extracting iron and



manganese from bacteria with ionophores - a mechanism against competitors characterized by increased potency in environments low in micronutrients, *Proteomics*, 2013, **13**(8), 1358–1370, DOI: [10.1002/PMIC.201200556](https://doi.org/10.1002/PMIC.201200556).

65 Y. Yang, Y. Hu, H. Du and H. Wang, Intracellular gold nanoparticle aggregation and their potential applications in photodynamic therapy, *Chem. Commun.*, 2014, **50**(55), 7287–7290, DOI: [10.1039/C4CC02376E](https://doi.org/10.1039/C4CC02376E).

66 M. K. Khaing Oo, X. Yang, H. Du and H. Wang, 5-aminolevulinic acid-conjugated gold nanoparticles for photodynamic therapy of cancer, *Nanomedicine*, 2008, **3**(6), 777–786, DOI: [10.2217/17435889.3.6.777](https://doi.org/10.2217/17435889.3.6.777).

67 S. N. S. Khan, S. N. S. Khan, R. Meena, A. M. Dar, R. Pal and A. U. Khan, Photoinactivation of multidrug resistant bacteria by monomeric methylene blue conjugated gold nanoparticles, *J. Photochem. Photobiol., B*, 2017, **174**(June), 150–161, DOI: [10.1016/j.jphotobiol.2017.07.011](https://doi.org/10.1016/j.jphotobiol.2017.07.011).

68 N. L. Pacioni, M. Gonzalez-Bejar, E. Alarcon and K. L. McGilvray JCS, Surface plasmons control the dynamics of excited triplet states in the presence of gold nanoparticles, *J. Am. Chem. Soc.*, 2010, **132**, 6298–6299, DOI: [10.1021/ja101925d](https://doi.org/10.1021/ja101925d).

69 A. Guerrero-Martínez, S. Barbosa, I. Pastoriza-Santos and L. M. Liz-Marzán, Nanostars shine bright for you: Colloidal synthesis, properties and applications of branched metallic nanoparticles, *Curr. Opin. Colloid Interface Sci.*, 2011, **16**(2), 118–127, DOI: [10.1016/J.COCIS.2010.12.007](https://doi.org/10.1016/J.COCIS.2010.12.007).

70 I. C. J. Zanin, M. M. Lobo, L. K. A. Rodrigues, L. A. F. Pimenta, J. F. Höfling and R. B. Gonçalves, Photosensitization of in vitro biofilms by toluidine blue O combined with a light-emitting diode, *Eur. J. Oral Sci.*, 2006, **114**(1), 64–69, DOI: [10.1111/J.1600-0722.2006.00263.X](https://doi.org/10.1111/J.1600-0722.2006.00263.X).

71 R. A. Harper, G. H. Carpenter, G. B. Proctor, *et al.*, Diminishing biofilm resistance to antimicrobial nanomaterials through electrolyte screening of electrostatic interactions, *Colloids Surf., B*, 2019, **173**, 392–399, DOI: [10.1016/J.COLSURFB.2018.09.018](https://doi.org/10.1016/J.COLSURFB.2018.09.018).

72 H. Nakamura and K. Takada, Reactive oxygen species in cancer: Current findings and future directions, *Cancer Sci.*, 2021, **112**(10), 3945, DOI: [10.1111/CAS.15068](https://doi.org/10.1111/CAS.15068).

73 M. Takeo, W. Lee and M. Ito, Wound Healing and Skin Regeneration, *Cold Spring Harbor Perspect. Med.*, 2015, **5**(1), a023267, DOI: [10.1101/CSHPERSPECT.A023267](https://doi.org/10.1101/CSHPERSPECT.A023267).

74 S. Mohsen, J. A. Dickinson and R. Somayaji, Update on the adverse effects of antimicrobial therapies in community practice, *Can. Fam. Physician*, 2020, **66**(9), 651–659, <https://www.ncbi.nlm.nih.gov/pmc/articles/PMC7491661/>, accessed October 3, 2023.

